JGR Biogeosciences

RESEARCH ARTICLE
10.1029/2019JG005289

Towards a Harmonized Long-Term Spaceborne Record of Far-Red Solar-Induced Fluorescence

Nicholas C. Parazoo[1], Christian Frankenberg[2], Philipp Köhler[2], Joanna Joiner[3], Yasuko Yoshida[3,4], Troy Magney[2], Ying Sun[5], and Vineet Yadav[1]

[1]Jet Propulsion Laboratory, California Institute of Technology, Pasadena, CA, USA, [2]California Institute of Technology, Pasadena, CA, USA, [3]NASA Goddard Space Flight Center, Greenbelt, MD, USA, [4]Science Systems and Applications, Inc., Lanham, MD, USA, [5]School of Integrative Plant Science, Soil and Crop Sciences Section, Cornell University, Ithaca, NY, USA

Abstract Far-red solar-induced chlorophyll fluorescence (SIF) has been retrieved from multiple satellites with nearly continuous global coverage since 1996. Multiple official and research-grade retrievals provide a means for cross validation across sensors and algorithms, but produces substantial variation across products due to differences in instrument characteristics and retrieval algorithm. The lack of a consistent, calibrated SIF data set hampers scientific interpretation of planetary photosynthesis. NASA's Orbiting Carbon Observatory 2 (OCO-2) offers small sampling footprints, high data acquisition, and repeating spatially resolved targets at bioclimatically diverse locations, providing a unique benchmark for spaceborne sensors traceable to ground data. We leverage overlap between the longer running Global Ozone Monitoring Instrument version 2 (GOME-2) SIF time series, and more recent state-of-the-art OCO-2 and TROPOspheric Monitoring Instrument (TROPOMI) data, in a first attempt to reconcile inconsistencies in the long-term record. After screening and correcting for key instrument differences (time of day, wavelength, Sun-sensor geometry, cloud effects, footprint area), we find that Global Ozone Monitoring Instrument version 2 and TROPOspheric Monitoring Instrument perform exceedingly well in capturing spatial, seasonal, and interannual variability across OCO-2 targets. However, Global Ozone Monitoring Instrument version 2 retrieval methods differ by up to a factor of 2 in signal-to-noise and magnitude. Magnitude differences are largely attributed to retrieval window choice, with wider windows producing higher magnitudes. The assumed SIF spectral shape has negligible effect. Substantial research is needed to understand remaining sensitivities to atmospheric absorption and reflectance. We conclude that OCO-2 and TROPOspheric Monitoring Instrument have opened up the possibility to produce a multidecadal SIF record with well-characterized uncertainty and error quantification for overlapping instruments, enabling back-calibration of previous instruments and production of a consistent, research-grade, harmonized time series.

Key Points:
- Accounting for illumination effects, Sun-sensory geometry, and uniform vegetation improves consistency across SIF data sets
- TROPOMI and GOME-2 SIF data sets compare well to OCO-2 target data, which are traceable to ground observations
- Retrieval algorithm differences in GOME-2 SIF magnitude and signal-to-noise largely attributed to length of retrieval window

Correspondence to:
N. C. Parazoo,
nicholas.c.parazoo@jpl.nasa.gov

Citation:
Parazoo, N. C., Frankenberg, C., Köhler, P., Joiner, J., Yoshida, Y., Magney, T., et al. (2019). Towards a harmonized long-term spaceborne record of far-red solar-induced fluorescence. *Journal of Geophysical Research: Biogeosciences*, *124*, 2518–2539. https://doi.org/10.1029/2019JG005289

Received 5 JUN 2019
Accepted 15 JUL 2019
Accepted article online 25 JUL 2019
Published online 14 AUG 2019

1. Introduction

Our ability to measure photosynthesis, one of the most important biological processes on Earth, at scales beyond a leaf is extremely limited. Consequently, there is substantial uncertainty in predicting the response and feedback of gross primary production (GPP) to climate change and, thus, carbon flux monitoring. Global remote sensing of solar-induced chlorophyll fluorescence (SIF) represents a major breakthrough in alleviating this deficiency. SIF originates from the core of photosynthetic machinery, in which a small fraction of light absorbed by chlorophyll is re-radiated as fluorescence at longer wavelengths (660–850 nm) and has been widely applied in photosynthesis research using modulated active light sources for decades (Baker, 2008; Genty et al., 1989; Krause & Weis, 1991; Moya et al., 2004). SIF, as measured by satellites, places constraints on photosynthetic activity, and has potential to offer more mechanistic understanding of ecosystem carbon dynamics (Christian Frankenberg, Fisher, et al., 2011; Flexas et al., 2002; Magney, Bowling, et al., 2019). However, multiple and considerable challenges (summarized below) have hindered progress toward this goal.

The SIF emission spectrum consists of two characteristics peaks in the red near 680 nm and far-red near 740 nm (Figure 1). Spaceborne observations of top-of-canopy (TOC) far-red SIF, ranging from 720 to 780 nm, have become widely available in recent years from instruments including the Greenhouse Gases Observing SATellite (GOSAT), Global Ozone Monitoring Instrument (GOME) onboard ERS-2 and its successor GOME-2 onboard MetOp-A, MetOp-B, and MetOp-C (this study focuses on the first two

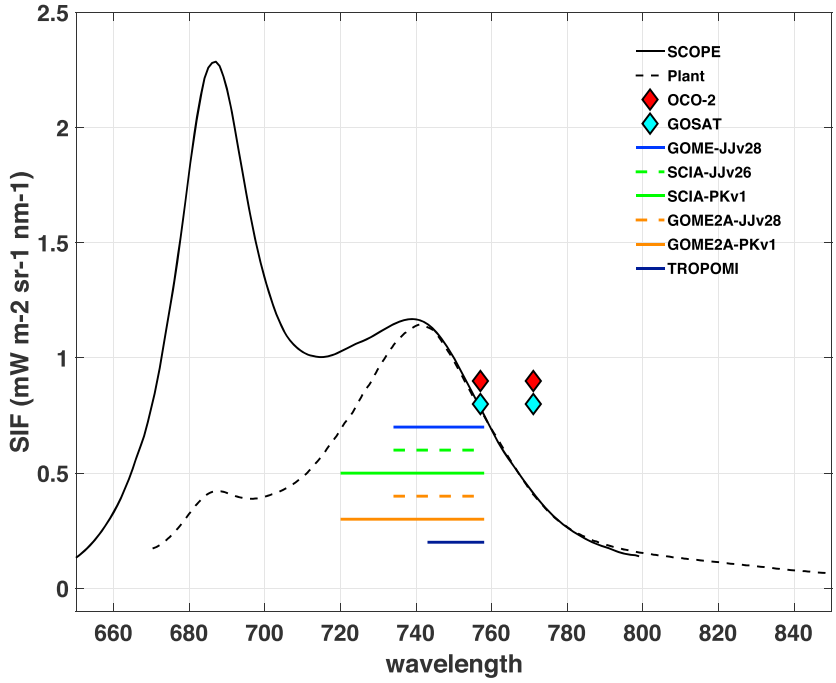

Figure 1. Simulated and observed SIF spectral shape and satellite retrieval windows. The SCOPE spectral shape (solid) occurs at the photosystem level and does not account for reabsorption by chlorophyll (raw emission). Observed spectral shapes obtained from leaf fluorescence spectra account for reabsorption by chlorophyll and thus reduced magnitude compared to SCOPE. Horizontal lines and diamonds represent the wavelength region where satellite retrievals are performed. Individual sensors are color coded, and retrieval algorithms indicated by solid or dashed lines.

sensors, denoted GOME2A and GOME2B, respectively), SCanning Imaging Absorption SpectroMeter for Atmospheric CHartographY (SCIAMACHY) onboard ENVISAT, Orbiting Carbon Observatory 2 (OCO-2), and TROPOspheric Monitoring Instrument (TROPOMI; Christian Frankenberg, Fisher, et al., 2011; C Frankenberg, Butz, et al., 2011; Guanter et al., 2012; Joiner et al., 2011, 2012, 2013; Köhler, Guanter, et al., 2018; Köhler et al., 2015). Together, these instruments provide a continuous record of SIF extending from 1995 with GOME, through 2012 with SCIAMACHY, and up to the present with GOME-2, OCO-2, and TROPOMI (Figure 2). However, none were specifically designed for dedicated SIF measurements. Rather, SIF observations were enabled in a fortuitous manner as the spectral range covering the Oxygen *A* band at 760 nm is often used in atmospheric remote sensing for cloud detection (Fischer et al., 1991) and to account for scattering effects in the atmosphere (Crisp et al., 2004). Their design parameters are thus optimized for the observation of atmospheric trace gas constituents rather than the land surface, which is why the spatial and temporal sampling are coarser than dedicated vegetation remote sensing missions.

Consequently, for SIF retrievals, mismatches in spectral, temporal, and spatial resolution across sensors; differences in retrieval algorithm methods; and sensor degradation create significant challenges for robust ground validation, radiance calibration, algorithm development and testing, spatial and daily integration, and long-term trend analysis. These mismatches can lead to substantial differences in retrieved SIF spatio-temporal variability over a given region without proper cloud screening and corrections applied (e.g., Köhler, Frankenberg, et al., 2018). Many of the corresponding limitations of these sensors are known and acknowledged by data set developers (e.g., https://avdc.gsfc.nasa.gov/pub/data/satellite/MetOp/GOME_F/README_GOME-F_v26-v27.pdf GOME-2 FLOURESCENCE README FILE, "should not be used for trend analysis"), but often unknown, unaccounted for, or ignored by the user community. There remains substantial uncertainty in vegetation and remote sensing communities as to whether TOC fluorescence emissions can be accurately estimated from spaceborne passive sensors. As such, the full potential of existing SIF records to quantify and understand long-term photosynthetic change has not yet been fully realized. We outline some of the primary spatial, temporal, spectral, algorithmic differences below (we refer the reader to Guanter et al. (2015) for more detailed discussions) and discuss several recent experiments, advances in

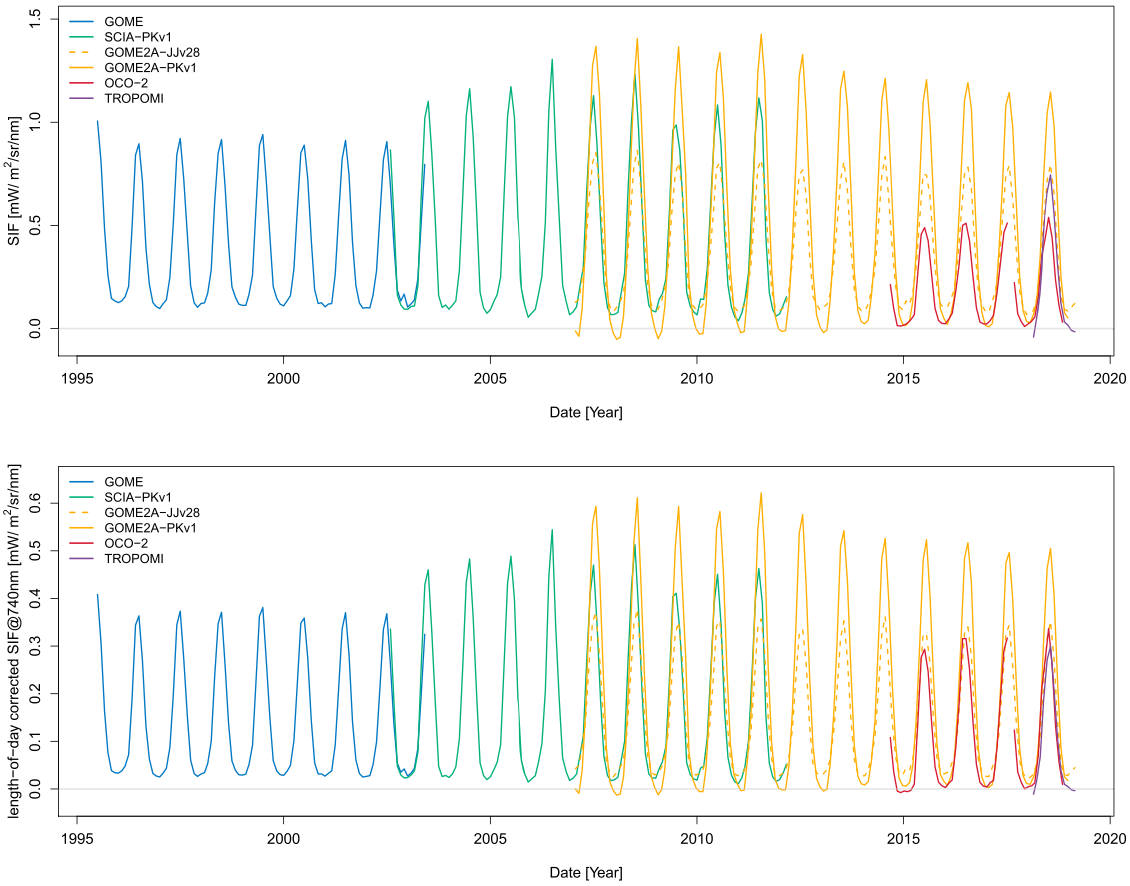

Figure 2. Time series of (top) instantaneous and (bottom) corrected (length-of-day and wavelength) SIF for all sensors averaged from 30 to 60°N over the period 1995–2018. Color coding and line style are consistent with Figure 1.

retrieval methodology enabled by recently launched sensors, and ground validation opportunities that have helped to assuage some of these uncertainties.

1.1. Spatial Characteristics

Footprint size has substantial variation between instruments, with area scales differing by a factor of 10^2 to 10^4 between high and moderate spectral resolution instruments, and by a factor 10 between instruments of the same spectral resolution. However, there are trade-offs between spectral resolution, footprint size, and spatial sampling. For example, wide-swath sensors such as GOME, SCIAMACHY, and GOME-2 provide nearly continuous spatial mapping, but the effective sampling footprints in the far-red are relatively coarse (40×320, 30×120, and 40×40 km^2, respectively) and challenge interpretation under mixed vegetation landscapes and atmospheric conditions. To complicate matters further, GOME has a small swath mode every one to two days per month with 40×80-km^2 pixels, which requires unique interpretation relative to the larger pixels in its nominal swath mode. Likewise, GOME2A underwent a change in the swath width on 15 July 2013 which permanently reduced its sampling footprint from 40×80 km^2 at nadir prior to 15 July 2013 to 40×40 km^2 afterward (with a smaller swath width), while GOME2B continues to observe in the larger swath mode at 40×80 km^2. We note that the native footprint of SCIAMACHY in the O2-A band where far-red SIF is found is actually 30×60 km^2, but the effective footprint is increased by a factor of 2 (30×120 km^2) due to onboard averaging of radiances in the O2-A band.

OCO-2 and GOSAT have small footprints (1.3×2.25 km^2 and 10 km in diameter, respectively) closer to the scale of flux towers (~1–2 km), but GOSAT's sparse data acquisition and OCO-2's narrow swath width prevent continuous spatial mapping. TROPOMI offers many of the advantages of these sensors, including high observational density (4.2-M soundings per day), continuous spatial mapping, and spatial resolution

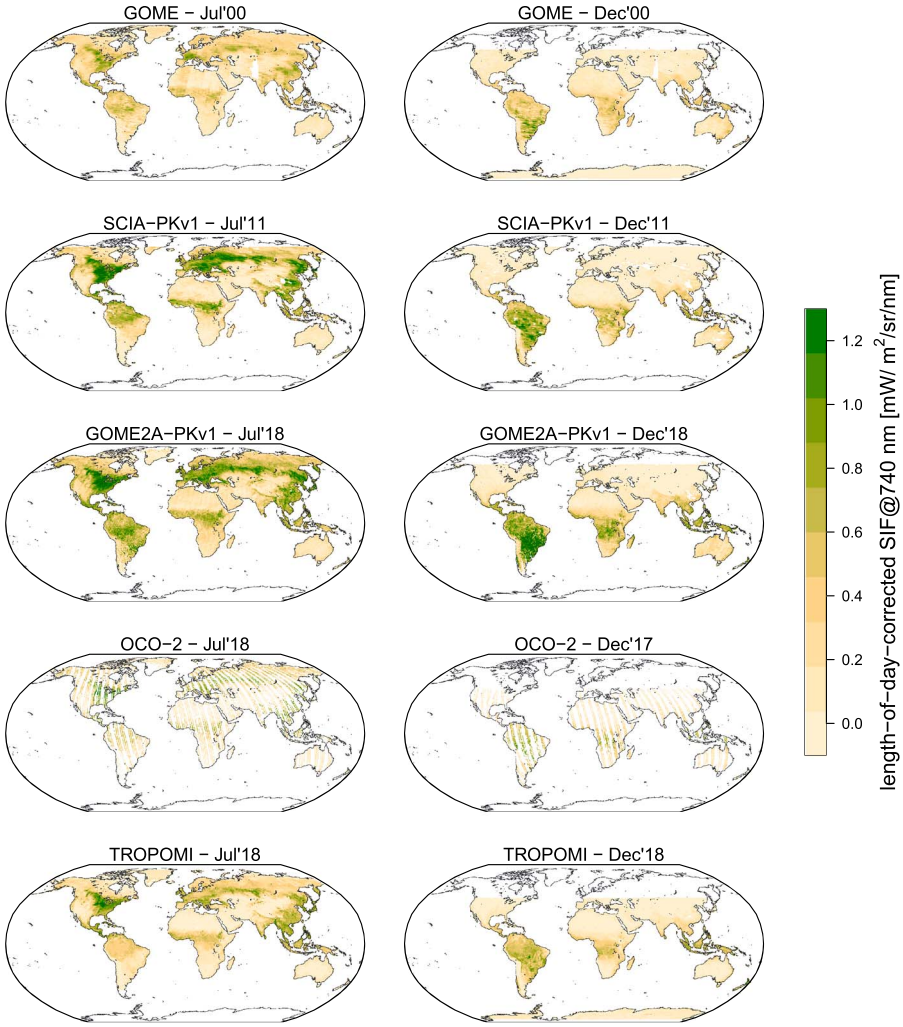

Figure 3. Monthly mean maps of length-of-day corrected SIF for all satellite sensors averaged for (left) July and (right) December. This shows differences between sensors in spatial coverage, spatial resolution, and magnitude.

(3.5×7 km^2 at nadir) converging on that of OCO-2. Figure 3 shows the substantial difference in the spatial mapping between wide-swath sensors (GOME, GOME-2, SCIAMACHY, TROPOMI) and OCO-2.

1.2. Temporal Characteristics

Additional complications arise in that each sensor provides only a single daily overpass (wide-swath sensors at higher latitudes are an exception). This prevents accurate estimation of daily-averaged SIF because the SIF yield varies with changing light conditions (e.g., Magney, Frankenberg, et al., 2019; Yang et al., 2015). Overpass times differ between sensors (morning for GOME, GOME-2, and SCIAMACHY; midday for GOSAT, OCO-2, TROPOMI), which further confounds sensor intercomparison and cross calibration (e.g., Figure 2a), and adds uncertainty when analyzing vegetation photosynthetic responses across optical vegetation indices due to differences in diurnal stress patterns (Zhang, Xiao, et al., 2018). We also note substantial differences in the revisit cycle of instruments, ranging from nearly daily for wide swath sensors, up to 5 days for GOSAT, and 16 days for OCO-2. As such, wide-swath sensors can be intercompared at submonthly resolution, but monthly averaging is required for comparison to GOSAT and OCO-2 nadir and glint modes.

1.3. Spectral Characteristics and Retrieval Method

SIF retrieval methods implemented for satellite instruments have primary utilized in-filling of solar Fraunhofer lines since the advent of GOSAT in 2009. However, differences in spectral ranges and

resolutions between sensors prevent the use of a single retrieval algorithm for all sensors. This has led to the development of distinctly different retrieval methods. GOSAT and OCO-2 measure isolated solar Fraunhofer lines in narrow spectral windows at 757 and 771 nm, enabled by the high spectral resolution (<0.05 nm) in the O2-A band channel (e.g., Frankenberg, Fisher, et al., 2011). GOME, GOME-2, SCIAMACHY, and TROPOMI measure in wider spectral windows in the far-red but at coarser spectral resolution. To get good-quality retrievals with lower spectral resolution, a wider spectral fitting window is used that typically encompasses wavelengths closer to the far-red emission peak. Atmospheric water vapor may absorb radiation at some of these wavelengths. Use of the larger fitting windows therefore typically requires more complicated statistical retrieval techniques.

1.4. Retrieval Method for High Spectral Resolution (<0.2 nm)

The first SIF retrievals from space were performed independently by Joiner et al. (2011) and Frankenberg, Butz, et al. (2011) using data from GOSAT. Their retrieval technique uses very small (~2 nm) microwindows centered around 757 or 771 nm, covering solar Fraunhofer lines with negligible overlapping atmospheric absorption. The use of microwindows for disentangling SIF signals from the background is very robust and insensitive to atmospheric scattering (Frankenberg et al., 2012), and compares well against airborne observations (Frankenberg et al., 2018; Sun et al., 2017).

1.5. Retrieval Method for Coarse Spectral Resolution (~0.5 nm)

In order to improve on GOSAT coarse spatial coverage and temporal revisit time, methods for retrieval of SIF from lower spectral resolution spectrometers were developed. For these sensors, wider spectral windows are needed to retrieve SIF with good fidelity that can make the retrievals more susceptible to confounding effects from the atmosphere and surface. This requires more complicated statistical modeling approaches to separate SIF emissions from spectral features related to atmospheric absorption, scattering, and surface reflectance. There are two main approaches which are related in the derivation of spectral basis functions using singular value decomposition (SVD) and differ primarily in technical detail.

The first approach, developed and refined by Joiner et al. (2013, 2016), has the following defining characteristics: (1) a relatively narrow fitting window (734–758 nm) that contains fairly weak water vapor absorption, (2) a fourth-order polynomial to describe surface reflectance, and (3) a fixed number of principal components (PCs) to describe atmospheric absorption and other instrumental artifacts. This approach adjusts for known biases (e.g., stray light and dark current) identified by Köhler et al. (2015) using data over oceans where SIF is negligible. It has been applied using data from GOME, SCIAMACHY (denoted SCIA-JJv26), and GOME-2 Met-Op A (GOME2A-JJv28) and Met-Op B (GOME2B-JJv28).

The second approach developed by Köhler et al. (2015) as a variant of Joiner et al. (2013) combines a third-order polynomial in wavelength with atmospheric PCs and a reference SIF emission spectrum to model low- and high-frequency components of the TOA radiance spectrum (720–758 nm) in a linear way. Consequently, the linear forward model permits a backward elimination algorithm, selecting the required model parameters automatically with respect to goodness of fit balanced by model complexity. This approach provides a solution for an arbitrary selection of a fixed number of model parameters. The backward elimination algorithm ensures stable results, regardless of how many atmospheric PCs are initially provided to the retrieval. Results suggest (i) using far fewer PCs (8) than GOME2A-JJv28 and SCIA-JJv26 (12) and (ii) noise is reduced by selecting a subset of initial model parameters (overfitting is avoided). This approach as applied to SCIAMACHY and GOME2 is denoted SCIA-PKv1 and GOME2A-PKv1, respectively.

Results obtained with satellite retrievals using the SVD method show good agreement across sensors in the seasonal cycle, and only moderate cloud effects on cloud-filtered data sets (Frankenberg et al., 2012; Guanter et al., 2015; Köhler et al., 2015). Results from Köhler et al. (2015) also show that seasonality is maintained in agreement with physical-based approaches with respect to GOSAT (Guanter et al., 2012; Köhler et al., 2015) and OCO-2 (Köhler, Guanter, et al., 2018). Cloud-free scenes should be used as much as possible for cross-sensor analyses, especially for sensors with significantly different footprint size. However, even after cloud screening, comparison with GOME2A-JJv28 reveals substantial difference in absolute values, up to a factor of 2 as seen in Figure 2a. These absolute differences have important consequences for SIF interpretation and assimilation in land surface models (Norton et al., 2018) especially those relying on GOME-2 (MacBean et al., 2018).

For instruments with moderate spectral resolution but high signal to noise, there exists a relatively small spectral window in the far red from 745 to 758 nm (mostly) devoid of atmospheric absorption features and high relative SIF for improved accuracy (Guanter et al., 2015). TROPOMI features the required spectral resolution (~0.5 nm) and high SNR in the 742–758 retrieval window (2,660) to enable accurate SIF retrievals in this window while also achieving higher spatial resolution compared to GOME, SCIAMACHY, and GOME-2 (Köhler, Frankenberg, et al., 2018). For comparison, SCIAMACHY has SNR up to 3,000 and GOME-2 up to 2,000, while OCO-2 ranges from 200 to 700 and GOSAT is less than 200 (Frankenberg et al., 2014). Retrieval estimates based on an SVD approach similar to Köhler et al. (2015) show excellent agreement with OCO-2 at global scale (Köhler, Guanter, et al., 2018).

To further demonstrate the validity of the SVD method for TROPOMI, an experiment was conducted in which an artificial SIF signal including randomly varying spectral shapes and noise was added to a single data of real TROPOMI measurements (Köhler, Frankenberg, et al., 2018. The added noise patterns had a predictable effect on the retrieved artificial SIF signal (cf. Figure S5) in that the precision is consistent with the prediction. This demonstrates that a significant dynamic range in radiance levels, related to albedo effects such as clouds, snow, and vegetation, do not lead to retrieval artifacts in the TROPOMI signal.

1.6. Spectral Shape

Another important question regarding SIF retrievals is whether the reference SIF emission shape is correlated with other spectral functions used in the retrieval in a way that affects the retrieval accuracy and precision leading to location-dependent biases. Leaf-level spectral measurements show relatively weak variability across species and conditions in the SIF emission spectrum near the far-red peak (~740 nm), and high variability across the red peak (~680 nm; Magney, Frankenberg, et al., 2019). The shorter far-red spectral window used for TROPOMI is stable with respect to changes in the shape of the fluorescence emission spectrum, as suggested by leaf-level spectral measurements. Leaf-level measurements also show a similar SIF spectral shape to SCOPE simulations (Van Der Tol et al., 2014) near 740 nm (Figure 1), which is encouraging given the use of SCOPE to derive reference SIF shapes for statistical modeling approaches. We note that methods that use wider retrievals windows extending to 720 nm, such as SCIA-PKv1 and GOME2A-PKv1, may experience increased sensitivity to SIF reference spectra as observed and simulated spectral shapes diverge moving closer to the red spectral region (Figure 1). Sensitivity to SIF reference spectra is discussed in more detail in Sections 2.4 and 3.4.

1.7. Canopy Scattering

Another factor that should be taken into consideration is the scattering of SIF in the far red (Yang & van der Tol, 2018). That is, SIF emitted from leaves can be scattered and reabsorbed by other leaves, leading to differences between leaf-level SIF and TOC SIF observed by the satellite. Although this should have limited effect on individual SIF retrievals, this can affect SIF intercomparisons for different spatial resolution at heterogeneous landscape due to the different scattering coefficient in the far red.

1.8. Wavelength

Existing satellite retrieval methods typically report estimated SIF at a reference wavelength of 740 nm for moderate spectral resolutions and at 757 or 771 nm for high spectral resolutions. This may confound intersensor comparisons such as in Figure 2a. The choice of 740 nm is used because it is near the peak of the SIF emission feature in the far-red. The choice of 757 or 771 nm as a reference wavelength for OCO-2 and GOSAT is driven by (1) the ability to perform narrow band retrievals and (2) the lack of larger spectral regions capable of performing SIF retrievals. Although the intersensor wavelength range is relatively small (~30 nm), absolute fluorescence values vary by more than a factor of 2 in this region (Joiner et al., 2013; Köhler, Guanter, et al., 2018; Sun et al., 2018). Reference SIF shapes derived from leaf-level studies suggest that far-red fluorescence spectra, and thus wavelength conversions, are roughly consistent across species (Magney, Frankenberg, et al., 2019). In principle, a look-up table approach could be used to determine a multiplicative factor to convert between different wavelengths evaluated across sensors/retrievals based on a reference spectrum derived from an average across multiple plant species.

1.9. Atmospheric Scattering

Atmospheric scattering by aerosols and clouds is a well-known source of uncertainty for reflectance-based vegetation products. A major appeal of spaceborne SIF is the very low sensitivity to scattering (C. Frankenberg, Butz, et al., 2011). More than 80% of TOC emitted SIF reach the sensors for clouds with low to moderate optical thickness (up to 5; Frankenberg et al., 2012). The effect of attenuation under high optical depth was examined in more detail using simulation experiments of OCO-2 spectra under realistic conditions, and supported empirical evidence that TOA SIF signals are only marginally reduced under moderate optical densities and/or low single scattering albedo (Frankenberg et al., 2014). Optically thick clouds (up to 10 and above) can severely attenuate the SIF signal. Retrievals under these conditions may be filtered out through preprocessor and postprocessor cloud screening (Köhler, Frankenberg, et al., 2018; O'Dell et al., 2012).

1.10. Other Sensor Characteristics

A number of other confounding factors exist for individual sensors. Retrieved SIF magnitudes are sensitive to absolute radiance (or irradiance) calibration, and therefore, SIF signals retrieved with a consistent algorithm using different sensors (e.g., GOME and GOME-2) show a bias between the two; this is thought to be related to issues with absolution calibration of instruments. Instrument degradation over the lifetime of these sensors can also lead to long-term decreasing trends in SIF whose spatial pattern is independent from moisture gradients (Zhang, Joiner, Gentine & Zhou, 2018). These effects have led data providers to warn against the use of GOME, SCIAMACHY, and GOME-2 in particular for long-term trend analysis until degradation and calibration effects are more accurately accounted for in the SIF retrieval.

1.11. Illumination Effects

Another confounding factor for intersensor analyses is the response of far-red SIF to photosynthetically active radiation (PAR). For example, a comparison between GOME2A-PKv1 and OCO-2 in the Amazon basin reveals large-scale bimodal distribution of GOME-2 retrieved SIF, peaking first in February and again in October, while OCO-2 peaks a single time in February (Köhler, Frankenberg, et al., 2018). However, consistent seasonal cycles were found when normalized by illumination conditions and Sun-sensor geometry. To optimize the probability of multiple sensors observing a similar scene, we must correct for instantaneous illumination conditions (time of day, cloud interference, PAR), and directional effects, as discussed below.

To address instantaneous illumination effects, Frankenberg, Fisher, et al. (2011) proposed a normalization method which accounts for variations in overpass time, length of day, and SZA across time, space, and sensors (discussed in more detail in Köhler, Guanter, et al. (2018)). This normalization is a first-order approximation to the daily SIF average, and provides a correction for the overpass time-induced variation in clear-sky PAR and instantaneous SIF, with the following assumptions: (1) diurnal changes in incoming PAR are mostly determined by the SZA (e.g., changes in fluorescence yield across different instrument overpass times are negligible, and diurnal effects on fluorescence yield such as heat and water stress are constant throughout a particular day) and (2) cloud and atmospheric scattering effects on PAR are small after screening for clear-sky values. Normalization by SZA and length of day account for variation in the SIF daily average with latitude and season, and has a substantial impact on SIF seasonality especially at high latitudes (Sun et al., 2018). Moreover, Zhang, Xiao, et al. (2018) show improved agreement between satellite SIF and daily tower GPP when accounting for seasonal and latitudinal variations in PAR as approximated by SZA. Both studies support the use of SZA normalization as a first-order correction for instantaneous illumination. Correction for wavelength and illumination effects using the normalization equation above mitigates intersensor differences in magnitude across northern midlatitudes (Figure 2), specifically bringing OCO-2 into closer agreement with TROPOMI and GOME-2. However, differences due to second order environmental and scattering effects, and in particular retrieval method (e.g., GOME2A-JJv28 versus GOME2A-PKv1), are evident and require deeper investigation with respect to ground-based measurements of subdaily SIF (see below).

It is also important that cross-sensor analyses and calibration accurately account for Sun-sensor geometry. In particular, radiative hot spots are observed when the Sun and sensor are aligned along the same axis (e.g., Liu et al., 2016), which can lead to increases in retrieved SIF under decreasing illuminations (higher solar and viewing angles), and intensity changes of 20% relative to inclined phase angles (Köhler, Frankenberg et al., 2018). Fortunately, most observations are collected between 20 and 60° of solar angle, where the intensity change is less severe (~10%). Viewing zenith angle is also quite variable across sensors and can also affect

the fraction of illuminated leaves and thus emitted SIF observed. Multiple studies highlight the importance to take the seasonality of sun-sensor geometry into account when analyzing satellite vegetation data and in cross-sensor comparisons studies (Hilker et al., 2015; Maeda & Galvão, 2015; Morton et al., 2014; Verrelst et al., 2008).

To account for directional effects in comparing GOME2A-PK and OCO-2 in the Amazon, Köhler, Guanter, et al. (2018) calculated the phase angle (γ) by applying the spherical law of cosines:

$$\gamma = a\ \cos[\cos\theta_o \cos\theta_v + \sin\theta_o \sin\theta_v \cos(\phi_0 - \phi_v)]$$

This gives the angle between the directions to the Sun and detector, as seen from the surface, as a function of solar geometry (solar zenith angle (θ_o) + solar azimuth angle (ϕ_0)) and viewing geometry (viewing zenith angle (θ_v) + viewing azimuth angle (ϕ_v)). Kohler, Guanter, et al. (2018) limited the analysis of Amazon SIF to phase angles common across all seasons (−65 to −40°), revealing dynamical change in GOME-2 SIF more directly attributable to biophysical processes including changes in PAR during the dry season, and to leaf age and structural effects in the wet season (Köhler, Guanter, et al., 2018). Likewise, Köhler, Frankenberg, et al. (2018) analyzed collocated measurements of TROPOMI and OCO-2 at global scale by limiting phase angle differences to 20°. Phase angle is strongly variable geographically, diurnally, seasonally, and across sensors. As such, the choice of phase angle range depends on the application, the most important point being that low phase angles are close to the hot spot and will lead to higher SIF values (on the order of 20%).

1.12. Validation for Passive SIF Detection

Recent efforts have more directly addressed SIF detection uncertainty using Kautsky curve experiments to observe dark-light transitions. The well-known Kautsky effect, representing a change in fluorescence when vegetation is suddenly exposed to light after a period of dark (Kautsky and Hirsch, 1931), has been studied in the lab using pulse amplitude modulation fluorimetry to modulate photosystem II reaction centers for several decades (Krause & Weis, 1991), and more recently in the field (Grossmann et al., 2018). The idea is to reproduce the rapid change in fluorescence yield upon sudden illumination of dark adapted vegetation, related to activation of nonphotochemical quenching, thus providing a simple test that fluorescence instruments are indeed observing SIF.

Three experiments with three unique spectrometer systems demonstrate the utility of this approach. The first experiment was conducted in a lab using a blue light-emitting diode light to illuminate dark adapted plants show the characteristic peak and gradual relaxation of fluorescence (Yang et al., 2018). This experiment used the spectral fitting method and singular vector decomposition to retrieve SIF in the far-red. A second experiment was performed in the field on a banana leaf using Fraunhofer-line based retrievals acquired from PhotoSpec and simultaneous pulse amplitude modulation measurements of the same leaf to show a Kautsky curve response in red and far-red SIF yield (Grossmann et al., 2018). In this case, the plant was covered with a black cloth for 20–30 min then exposed to ambient sunlight (PAR = 1,430 μmol s^{-1} m^{-2}). An additional novelty is the use of a built-in telescope enabling the spectrometer to point directly at a sample leaf, and subsequently to scan over the entire canopy to establish robust leaf- to canopy-scaling relationships. A third experiment was also performed in ambient conditions using the Chlorophyll Fluorescence Imaging Spectrometer (CFIS). CFIS is an airborne high-resolution imaging spectrometer built at NASA JPL and designed specifically to retrieve SIF in the wavelength range and at high spectral resolution of OCO-2. Stationary acquisitions of covered and uncovered grass targets measuring rapid changes and relaxation of fluorescence yields, consistent with the Kautsky curve (Frankenberg et al., 2018).

1.13. Ground Validation

Efforts to increase consistency across sensors are limited without robust ground validation. Airborne acquisitions from CFIS in 2015, 2016, and 2017 in CONUS and in the NASA ABoVE domain in 2017 provided important validation opportunities for OCO-2. CFIS measurements show strong spatial gradients across diverse agricultural, natural, and urban landscapes (Frankenberg et al., 2016, 2018), enabling scaling from canopy-scale measurements to ecosystem-level data from spaceborne instruments. Airborne acquisitions on 13 and 15 August 2015 show remarkable agreement with OCO-2 during under-flights of OCO-2 orbital

nadir tracks in the Midwest United States, matching both in absolute value and in spatial variability (Sun et al., 2017).

Recent commercially available spectrometers have made it possible to measure SIF directly in the field over the canopy and study structural, environmental, and directional controls (Cogliati et al., 2015; Daumard et al., 2010; Grossmann et al., 2018; Migliavacca et al., 2017; Yang et al., 2015, 2018). The use of field deployable instruments on eddy covariance towers has increased rapidly since 2014, providing coverage of multiple vegetation types and climate gradients around the world (Magney, Bowling, et al., 2019; Yang et al., 2018). These data enable improved understanding of the relationship between SIF, photosynthesis, absorbed sunlight, and environmental effects at leaf to canopy scales. Novel ground-based spectrometer systems such as Fluospec2 (Yang et al., 2018), Photospec (Grossmann et al., 2018), and FLOX (e.g., Shan et al., 2019) have made it possible to monitor canopy SIF continuously in the field with high precision over multiple years providing opportunities for direct comparison and evaluation of satellite data (Grossmann et al., 2018; Magney, Bowling, et al., 2019; Yang et al., 2015, 2018).

1.14. Objectives of This Study

Recent multisensor analyses provide increasing support for the dynamical nature of retrieved satellite SIF. Kautsky curve experiments in the lab and in the field provide direct evidence of our ability to use tower and airborne remote sensing for passive retrieval of SIF. The advent of high spectral and spatial resolution sensors such as OCO-2 and TROPOMI, and experiments to understand inherent noise and bias patterns in retrieval methods, have provided increasing confidence in our ability to use spaceborne remote sensing for passive retrieval of SIF. Careful treatment of satellite data for seasonal changes in Sun-sensor geometry and cloud cover is key to disentangle canopy directional effects and atmospheric dilution effects from physiological-based controls. However, application of SVD approaches for coarse spectral instruments such as GOME-2 and SCIAMACHY produce substantial and persistent differences in the absolute value of retrieved SIF, even for the same instrument after correcting for wavelength and time of day (Figure 2b). Although the pattern of variability is consistent and encouraging, the absolute value difference can limit their use in carbon cycle applications.

For OCO-2, we have validated uncertainty estimates, which compare well with observed scatter within the data set, and provided the first reliable and successful SIF validation against CFIS (Frankenberg et al., 2018; Sun et al., 2017). The emergence of multiyear OCO-2 records that overlap with GOME-2 and TROPOMI, and rapidly expanding tower and airborne networks, has enabled new opportunities to validate and optimize spaceborne data sets. In the next section, we lay out a strategy to optimize spaceborne SIF data sets for production of long-term harmonized SIF time series, anchored by OCO-2 validation and calibration to ground measurements. Our strategy focuses on (1) direct OCO-2 SIF validation against overlapping ground and airborne data; (2) ensuring sensor consistency through screening and correction for illumination and wavelength differences; (3) evaluation of GOME-2 and TROPOMI SVD retrievals against OCO-2 target mode observations, which enable improved spatial mapping across a limited number of sites; and (4) SVD retrieval sensitivity analysis Table 1.

2. Methods

2.1. OCO-2 Targets

Further refinement of SIF retrievals from spaceborne sensors is most likely to be achieved through coordinated measurements from spaceborne, airborne, and ground-based platforms, providing a means to intercalibrate spaceborne retrievals. OCO-2 is currently the only instrument that provides small ground sampling footprints traceable to canopy-level measurements from spatially continuous airborne acquisitions and temporally continuous tower measurements (Verma et al., 2017; Wood et al., 2017). However, the use of ground-based data to directly validate OCO-2 Nadir and Glint viewing modes, representing the primary measurement modes over land, is challenging due to the narrow swath width ground tracks, and lack of direct flux tower overpasses.

OCO-2 Target Mode observations have been collected at discrete locations around the world since 2014 (Table 2) with the primary objective to validate column-integrated CO_2 retrievals. In Target Mode, OCO-2 views a designated location continuously, in a back-and-forth repeating manner, as the satellite passes

Table 1
Network of Ground-Based Towers With SIF Instrumentation

Site name	Instrument	Target	Location	Geolocation	Time period	Plant functional type
Niwot Ridge: **NR1**	**PhotoSpec**[1]	**OCO-2: 2018–present**	Colorado, USA	40.0329°N, 105.5464°W	17 March 17–present	Evergreen needleleaf
University of Michigan: **UMB**	**PhotoSpec**[1]	OCO-3: 2019	Michigan, USA	45.5598°N, 84.7138°W	18 June–present	Deciduous broadleaf
Coles Field: **ICC**	**PhotoSpec**[1]	N/A	Iowa, USA	42.4865°N, 93.5264°W	2017	Corn
Brooks Field: **ISB**	**PhotoSpec**[1]	N/A	Iowa, USA	41.9745°N, 93.6937°W	2017	Soybean
Old Black Spruce: **OBS**	**PhotoSpec**[1]	**OCO-2: 2019**	Canada	53.9872°N, 105.1178°W	18 September–present	Evergreen needleleaf
La Selva: **LSE**	**PhotoSpec**[1]	N/A	Costa Rica	10.4233°N, 84.0211°W	17 January–18 May	Tropical
Harvard: **HRV**	**FluoSpec**[2,3]	OCO-3: 2019	Massachusetts, USA	42.5378°N, 72.1715°W	13 March–present	Deciduous broadleaf
Howland: **HO1**	**FluoSpec2**[2]	OCO-3: 2019	Maine, USA	45.2041°N, 68.7402°W	18 June–2018	Temperate evergreen forest
UIUC Energy Farm: **UIUC**	**FluoSpec2**[2,3]	OCO-3: 2019	Illinois, USA	40.0658°N, 88.2084°W	16 August–present	Corn, soybean
Pace: **UVA**	**FluoSpec2**[2]	OCO-3: 2019	Virginia, USA	37.9229°N, 78.2739°W	17 March–present	Deciduous broadleaf
Toolik: **ICT**	**FluoSpec2**[2]	N/A	Alaska, USA	68.6068°N, 149.2958°W	17 June–present	Shrub (Tussock tundra)
Pinyon Juniper: **MPJ**	**FluoSpec2**[2]	OCO-3: 2019	New Mexico, USA	35.4385°N, 106.2377°W	18 March–present	Shrub (Pinyon-Juniper)
Santa Rita Grass: **SRG**	**FluoSpec2**[2,5]	OCO-3: 2019	Arizona, USA	31.7894°N, 110.8277°W	April 2019–present	Grassland
Santa Rita Mesquite: **SRM**	**FluoSpec2**[2,5]	OCO-3: 2019	Arizona, USA	31.8214°N, 110.8661°W	April 2019–present	Mesquite savanna
Santa Rita Creosote: **SRC**	**FluoSpec2**[2,5]	OCO-3: 2019	Arizona, USA	31.9083°N, 110.8395°W	April 2019–present	Ponderosa
Mead 1: **CSP1**	**FluoSpec2**[4]	OCO-3: 2019	Nebraska, USA	41.1651°N, 96.4766°W	2017–present	Crop (maize/soybean)
Mead 2: **CSP2**	**FluoSpec2**[4]	OCO-3: 2019	Nebraska, USA	41.1649°N, 96.4701°W	2018–present	Crop (maize/soybean)
Mead 3: **CSP3**	**FLoX** [6]	OCO-3: 2019	Nebraska, USA	41.1797°N, 96.4397°W	2018–present	Crop (maize/soybean)
Cornell Musgrave: **COR**	**Sun** [7]	OCO-3: 2019	New York, USA	42.7228°N, 76.6628°W	2018–present	Crop (corn)
KAEFS: **OKO**	**FluoSpec2** [8]	OCO-3: 2019	Oklahoma, USA	34.9846°N, 97.5223°W	2018–present	Grass (prairie; C3/C4)
Ozark: **MZO**	**FAME**[9]	OCO-3: 2019	Missouri, USA	38.7441°N, 92.2000°W	2018–present	Deciduous broadleaf
Hyytiala: **HYY**	**Castell** [10]	**OCO-2: 2017**	Finland	61.8474°N, 24.2948°E	2016–present	Evergreen needleleaf
Cherwon: **CRK**	**Ryu** [11]	OCO-3: 2019	South Korea	38.2013°N, 127.2506°E	2016–present	Crop (rice paddy)
Taehwa Mountain: **TNM**	**Ryu** [11]	OCO-3: 2019	South Korea	37.3049°N, 127.3177°E	2018–present	Evergreen needleaf
Jurong: **JRO**	**FluoSpec2**[12]	OCO-3: 2019	China	31.8068°N, 119.2173°E	2017–present	Crop (paddy rice)
CN-**SHQ**	**FluoSpec2**[12]	OCO-3: 2019	China	34.5203°N, 115.5894°E	2017–present	Crop (wheat/maize)
Manaus: **ATTO**	**Rotaprism** [13]	OCO-3: 2019	Brazil	2.1459°S, 59.0056°W	Future	Evergreen Broadleaf
Tapajos (km67)	Saleska[14]	OCO-3: 2019	Brazil	2.8567°S, 54.9589°W	2018-present	Evergreen Broadleaf
Xilinhot (XLH)	FluoSpec2[12]	OCO-3: 2019	Inner Mongolia	45.26°N, 115.38°E	2017-present	Grassland
Majadas de Tietar North (LM1)	**FLoX**[15]	OCO-3: 2019	Spain	39.9427-N, 5.7787-W	Feb 2017-Present	Savannah
Leinefelde (LEI)	**FLoX**[15]	OCO-3:2019	Germany	51.3282°N, 10.3678°E	May 2019-Present	Deciduous Broadleaf

Notes: Email contacts for different instruments and sites are as follows: [1]jochen@atmos.ucla.edu, [1]useibt@ucla.edu, [1]tmagney@caltech.edu, [2]xiyang@virginia.edu, [3]jtang@mbl.edu, [4]kaiyug@illinois.edu, [5]wksmith@email.arizona.edu, [6]asuyker1@unl.edu, [6]jgamon@gmail.com, [7]ys776@cornell.edu, [8]xiangming.xiao@ou.edu, [9]woodjd@missouri.edu, [9]lianhong-gu@ornl.gov, [10]joan.porcar@helsinki.fi, [11]ryuyr77@gmail.com, [12]yongguangzh@gmail.com, [13]jberry@carnegiescience.edu, [13]akorn@carnegiescience.edu, [14]saleska@email.arizona.edu, [15]mmiglia@bgc-jena.mpg.de.

overhead. This provides the capability to collect a large number of measurements where ground-based instruments also measure CO_2 and SIF. Target Mode data thus provide high-precision, high data yield ($>10^3$ cloud-free soundings per target), spatial coverage (20×20 km^2), and seasonal resolution at bioclimatic unique locations around the world needed for more direct comparison to ground-based SIF sensors (Figure 4).

Here we use OCO-2 targets in two novel ways. First, we leverage coordinated measurements of OCO-2 and PhotoSpec collected at a subalpine needleleaf forest flux tower in Niwot Ridge, CO (denoted US-NR1), to

Table 2
List of OCO-2 Target Locations Since 2014

Site name	Location	Geolocation	Number of targets	Plant functional type
Eureka	Canada	80.0533°N, 86.4165°W	4	Frozen
Sodankyla	Finland	67.36798°N, 26.633°E	17	Shrub/grass
Fairbanks	Alaska, USA	64.8560°N, 147.8346°W	16	Evergreen needleleaf
Hyytiala[a, b]	Finland	61.8462°N, 24.2958°E	5	Evergreen needleleaf
Old Black Spruce[a, c]	Saskatchewan, Canada	53.9872, 105.1178°W	1	Evergreen needleleaf
Bialystok[b]	Poland	53.217°N, 23.0126°E	10	Crop/mixed forest
Karlsruhe	Germany	49.100°N, 8.4380°E	11	Mixed forest
Orleans	France	47.965°N, 2.1125°E	16	Urban/crop
Park Falls	Wisconsin, USA	45.9448°N, 90.2725°W	27	Mixed forest
Niwot Ridge[a]	Colorado, USA	40.0329°N, 105.5464°W	8	Evergreen needleleaf
Lamont	Oklahoma, USA	36.6039°N, 97.4856°W	43	Grassland
Tsukuba	Japan	36.0513°N, 140.1215°E	20	Urban
Dryden	California, USA	34.958°N, 117.882°W	19	Desert
Caltech	California, USA	34.125°N, 118.05°W	33	Urban/Mediterranean
Izana	Tenerife	28.297°N, 16.5180°W	10	Open shrub
Manaus[b]	Manaus, Brazil	3.2133°S, 60.5983°W	4	Evergreen broadleaf
ASC	Ascension Island	7.9696°S, 14.3937°W	14	Open shrub
Darwin	Australia	12.375°S, 130.9167°E	24	Evergreen broadleaf
Reunion	Reunion Island	20.901°S, 55.485°E	23	Urban/evergreen broadleaf
Wollongong	Australia	34.4061°S, 150.8793°E	27	Urban/evergreen broadleaf
Lauder	New Zealand	45.039°S, 169.682°E	26	Crop

[a]Locations with ground-based SIF. [b]Discontinued targets. [c]New target in May 2019.

directly validate OCO-2, thus providing evidence that OCO-2 provides a robust platform for measuring seasonal dynamical change consistent with ground-based, canopy-integrated data. Second, we leverage high spatial coverage of global and diverse OCO-2 targets to provide an uncertainty assessment of TROPOMI. We note that OCO-2 target scanning produces widely varying solar and viewing geometries for a given location. As such, we screen OCO-2 targets for high solar and viewing zenith angles (SZA < 60, VZA < 60).

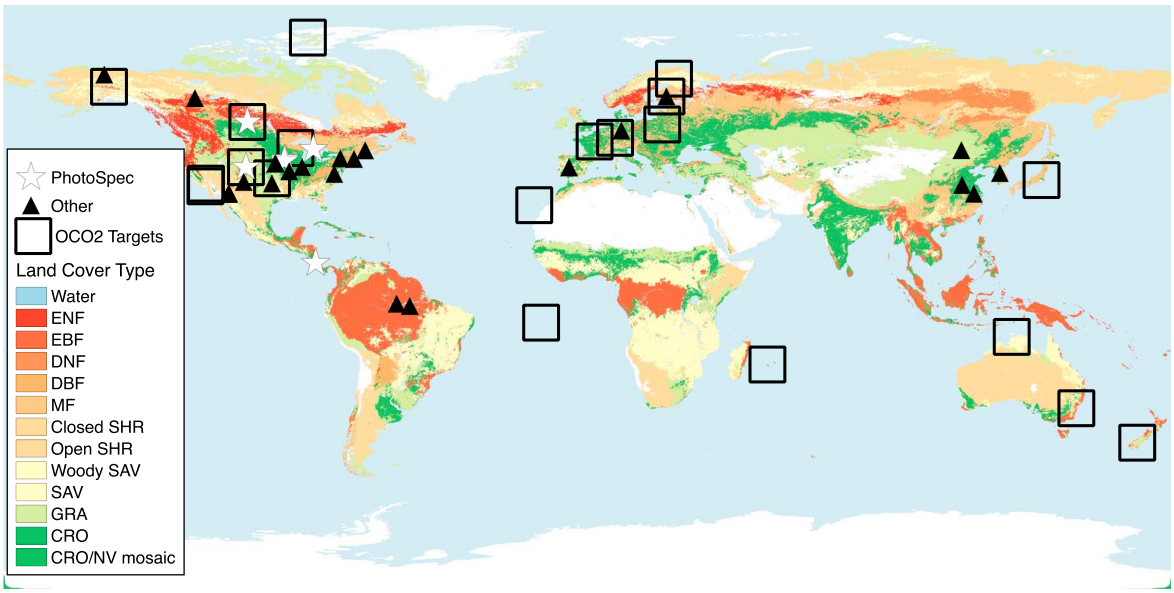

Figure 4. Map of tower network for ground-based SIF instrumentation and OCO-2 target locations. Table 1 provides more detail on site level SIF data.

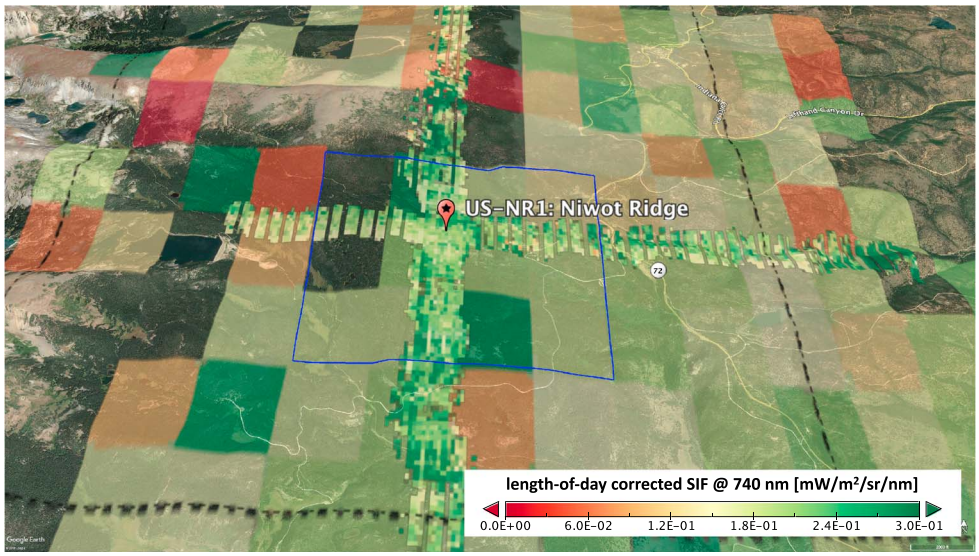

Figure 5. Map of SIF from OCO-2 targets (July 2018, background) and CFIS flights (June 2016, foreground) over Niwot Ridge flux tower. The marker labeled "NR1" denotes the Niwot Ridge flux tower where Photospec has been installed since August 2016. The blue rectangle represents a 4 × 4-km box of mostly uniform evergreen needleleaf vegetation. The 10–12 OCO-2 pixels fit within this box. OCO-2 and CFIS are length-of-day corrected at 740 nm and plotted on the same color bar.

2.2. OCO-2 Validation

OCO-2 targets have been collected at NR1 during the transition and growing seasons since April 2018, in coordination with CFIS flights in 2016 and ground-based data from Photospec since July 2017, to study needleleaf phenology and the timing and magnitude of seasonal GPP (Magney, Bowling, et al., 2019; Magney, 2019). Spectra from CFIS were collected during transient flights from California into the Midwest in June 2016.

Figure 5 provides an example of the high spatial coverage enabled by OCO-2 targets at NR1. Target data were collected as frequently as feasible (allowing for sufficiently low cloud cover and proximity of orbits) to resolve transition seasons, with particular emphasis on spring green-up and end of the growing season. OCO-2 targets were also collected in Hyytialla, Finland in 2018 as part of the Fluorescence Across Space and Time campaign, and new targets will begin in spring 2019 at the Old Black Spruce (CA-OBS) flux tower site in southern Saskatchewan, Canada, which was recently instrumented with PhotoSpec (Figure 4).

Ideally, such coordinated measurements provide additional opportunities for spaceborne validation and calibration, analysis of spatial gradients and mixed landscapes within a satellite pixel, and study of daily integration under different light and environmental conditions. In practice, the use of NR1 PhotoSpec data to validate spaceborne sensors is extremely challenging due to mixed vegetation and topography. Specifically, elevation changes at NR1 are drastic (~1,000 m in a few tenths of a degree) and vegetation transitions rapidly from tundra to evergreen needleleaf forests. The subgrid variability within coarse spatial footprints of GOME-2 is thus too high to allow for a robust validation study. Future measurements at OBS, which sits in a mostly flat landscape dominated by needleleaf evergreen forest, will provide more robust assessments of retrieval uncertainty and accuracy. In this study, we use NR1 PhotoSpec and CFIS data to assess the accuracy of smaller footprints from OCO-2 targets and TROPOMI.

2.3. OCO-2 Target Assessment of TROPOMI

Köhler, Guanter, et al. (2018) demonstrated high fidelity of TROPOMI SIF at global scale with respect to OCO-2 nadir data in June 2018. The authors analyzed points where at least 10 OCO-2 soundings fell within a TROPOMI footprint. OCO-2 targets provide the benefit of dense sampling over a relatively large area (20 km × 20 km) enabling improved signal to noise for TROPOMI and OCO-2. We extend the assessment of Köhler, Guanter, et al. (2018) using OCO-2 targets to analyze seasonal and spatial variability for the

period March–December 2018, and to assess sensitivity to time of day, wavelength, phase angle, and mixed vegetation.

For comparison to OCO-2 targets, TROPOMI data are selected for footprint centers falling within 0.2° of OCO-2 target centers. We account for differences in **atmospheric scattering** and **wavelength** using the clear-sky flag for OCO-2 and cloud fraction less than 0.1 for TROPOMI, and multiplying the OCO-2 757-nm band by a factor of 1.5 (based on our leaf-level spectral shape measurements) to match the TROPOMI 740-nm band. Using all OCO-2 data from 2014 to 2018 and TROPOMI data from 2018 as a starting point, we then iteratively correct for differences in (1) **year**, using 2018 data only; (2) **illumination**, by converting instantaneous values to daily averages using the length of day and SZA correction (e.g., Figure 2); (3) **Sun-sensor geometry**, by limiting phase angle differences to ±20°; and (4) **footprint size and canopy scattering**, by analyzing targets with uniform vegetation. Uniform vegetation is identified as target locations where greater than 50% of land cover is dominated by a single IGBP land cover type.

2.4. Retrieval Algorithm Testing and SIF Product Intercomparison

SIF retrieval amplitudes are substantially higher using the SVD method proposed by Köhler et al. (2015) than that proposed by Joiner et al. (2016) despite correction for time of day (Figure 2b). In addition to multiple technical differences, the difference most likely originates from the use of a relatively small fitting window (734–758 nm) in the most recent **Joiner** products (GOME-JJv28, SCIA-JJv26, GOME2-JJv28) compared to wider windows in the **Kohler** products (720–758 nm; SCIA-PKv1, GOME2-PKv1). Application of the **Kohler** method to TROPOMI provides an interesting sensitivity experiment; in that, many of the technical details are the same, but the use of a smaller window (742–758 nm) devoid of atmospheric absorption eliminates the use of solar irradiance data as another source of uncertainty, and significantly reduces SIF amplitudes while achieving high accuracy with respect to OCO-2 (Kohler, Frankenberg, et al., 2018).

A few possible explanations for the high bias of wider window lengths in the far-red include the following: (1) the assumed spectral shape of the SIF emission is incorrect (not accounting for reabsorption), (2) it is more difficult to fit the background reflectance and produce reliable principal components, and (3) the representation of water vapor absorption is inaccurate. In general, the wavelengths employed by **Joiner** have relatively weak water vapor absorption and tend to balance magnitude accuracy with reasonable signal to noise.

Comparison of length-of-day and wavelength-corrected SIF for GOME2A-PKv1, GOME2A-JJv28, and TROPOMI reveals a tendency for SIF magnitudes to decrease with smaller fitting windows weighted toward longer wavelengths near the far-red peak and in windows with less water vapor absorption (Figure 2). Specifically, we find decreasing SIF magnitude during the year 2018 moving to progressively narrow retrieval windows for GOME2A-PKv1 (720–758 nm), GOME2A-JJv28 (734–758 nm), and TROPOMI (742–758 nm). We further examine this sensitivity by applying the **Kohler** SVD method using narrower fitting windows. In the first experiment, GOME2A retrievals are performed using the 734–758-nm window to mimic the **Joiner** method. This is denoted as GOME2A-PKexp1. Another experiment is performed using the 742–758-nm window similar to the TROPOMI retrieval approach (Köhler, Guanter, et al., 2018), denoted GOME2A-PKtrop.

We also examine sensitivity to SIF reference shapes by substituting simulated estimates obtained from the SCOPE model (Van Der Tol et al., 2014; GOME2A-PKv1, GOME2A-PKexp1, and GOME2A-PKtrop) with observed shapes obtained from leaf fluorescence spectra (Magney, Frankenberg, et al., 2019). Leaf-level data account for reabsorption by chlorophyll across red and into the far-red wavelengths, and thus reduced magnitude up to 740 nm compared to photosystem-level emissions assumed by SCOPE (e.g., see Figure 1). Retrievals performed using the 720–758-nm window are denoted GOME2A-PKexp2, and using the 734–758-nm window as GOME2A-PKexp3.

We analyze GOME-2 retrievals and experiments against vegetation OCO-2 targets from 2015 to 2018, and against TROPOMI at global scale in July 2018, focusing on changes in slope, correlation, and magnitude. Our primary objectives are to benchmark **JOINER** and **KOHLER** GOME-2 retrievals against more accurate OCO-2 and TROPOMI data sets, and further explore underlying sensitivities of the retrieval.

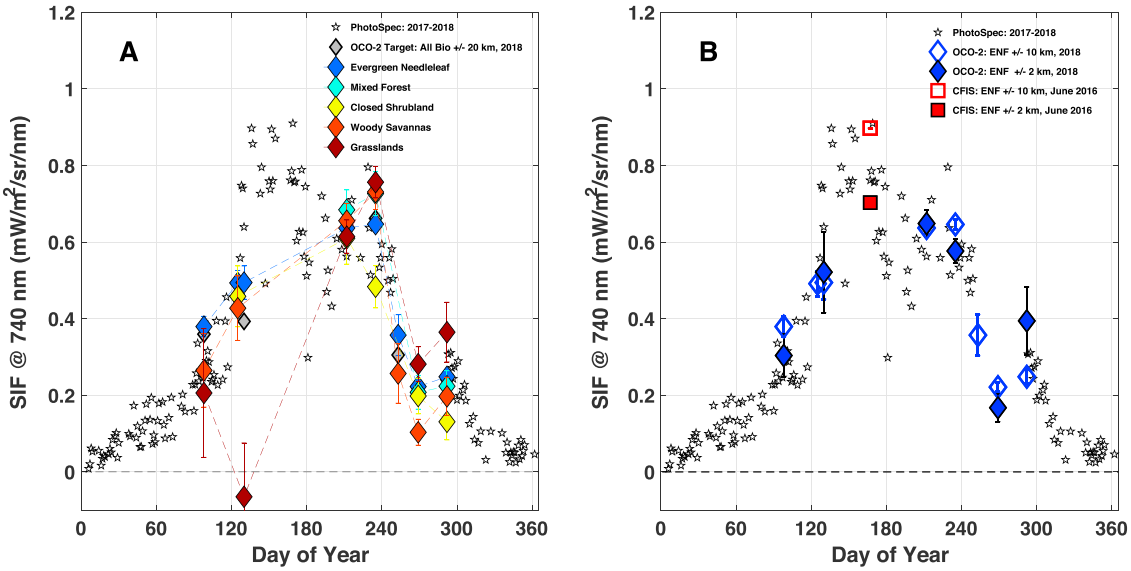

Figure 6. Seasonal time series of midday SIF remote sensing data from spaceborne (OCO-2), airborne (CFIS), and ground (PhotoSpec) platforms at Niwot Ridge, CO, corresponding to footprints shown in Figure 5. OCO-2 data, shown in diamonds, are distributed by (a) vegetation type and (b) by distance from tower. All data are collected during midday (12–2 pm local) and corrected to 740 nm. Substantial variability is seen in both cases, with evergreen needleleaf and distance of ±2 km from tower providing the best agreement with Photospec.

3. Calibration Results

We note three important points about the wavelength and time scale of intersensor comparisons in the following analysis: (1) all SIF data are reported at 740 nm, with OCO-2 757-nm band corrected by a factor of 1.5; (2) SIF data are either reported as instantaneous values or as daily average, with the latter identified as length-of-day corrected (e.g., Figures 7c–7e); and (3) no temporal averaging is applied, such that SIF values represent the time or day when the measurement was recorded.

3.1. Time Series Analysis: OCO-2 Comparison to Ground Data

PhotoSpec shows distinct seasonal characteristics including rapid spring transition, peak SIF early in the growing season, leveling off in the late growing season, and fall transition to dormancy (Magney, Bowling, et al., 2019; Figure 6). CFIS and OCO-2 values are directly in line with PhotoSpec, capturing absolute values and in particular the timing and amplitude of seasonal features including the rapid spring transition, relaxation of SIF following the spring peak, and rapid fall transition (Figure 6) after careful screening for biome (needleleaf forests) and clouds (sunny days only).

The comparison between OCO-2 and PhotoSpec also demonstrates the importance of screening for uniform vegetation, even for mostly homogeneous landscapes. NR1 is surrounded by needleleaf conifers within its 1–2-km footprint. Individual OCO-2 soundings (~2 km^2) are generally free of mixed canopies, but the larger target collection area (400 km^2) detects emissions from higher-altitude tundra and lower latitude deciduous forests 5–10 km away from the tower. In general, the target area is dominated by conifers, such that the mean signal of all soundings is within 5% of the mean signal from conifers. However, we note a significant influence of tundra toward the end of the spring transition, related to some combination of snow, bare soil, and relatively small signal emitted from grasses, which culminate in a low bias in the mean of OCO-2 soundings. This mixed landscape is likely to have an even greater impact on much coarser single sounding footprints from GOME-2, challenging the analysis of GOME-2 at NR1.

3.2. Retrieval Assessment: TROPOMI Comparison to OCO-2 Targets

TROPOMI shows high agreement with OCO-2 target data at nonurban land locations around the world, particularly at forest sites in northern latitudes (Figure 7). Specifically, comparison of overlapping TROPOMI and OCO-2 retrievals shows the increasing agreement in slope and correlation with iterative screening and corrections for confounding factors. We find high agreement already for instantaneous values

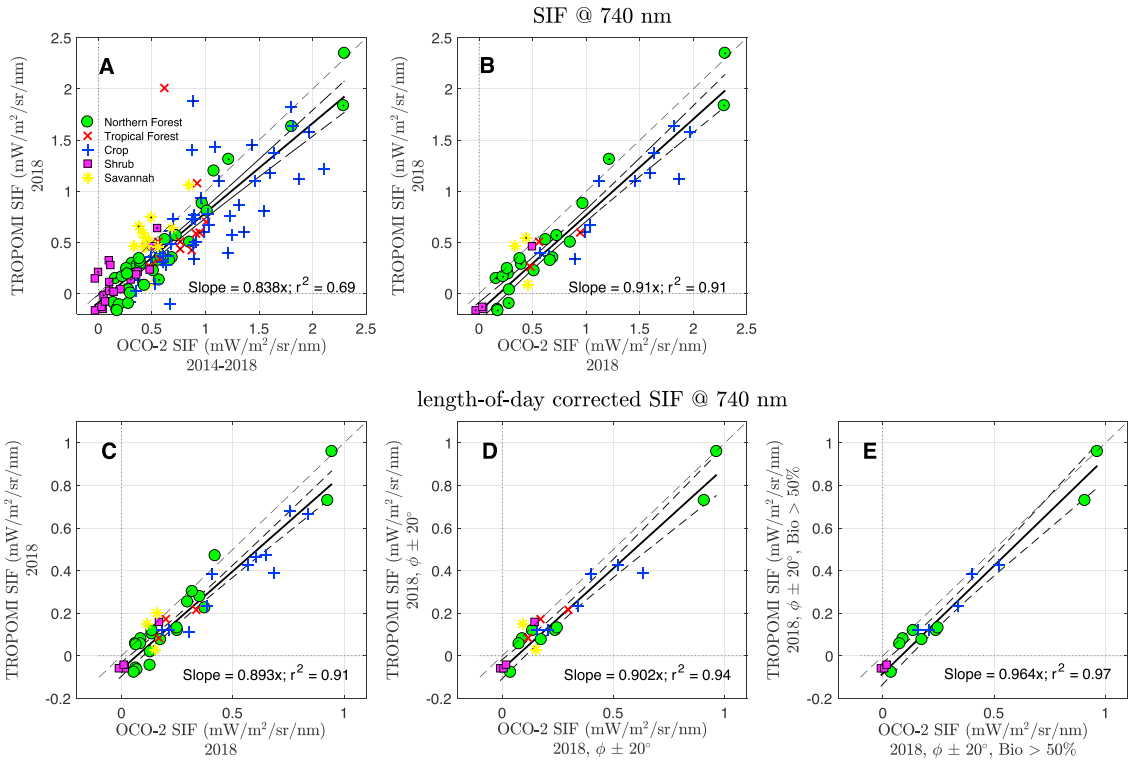

Figure 7. Regression of overlapping SIF retrievals from TROPOMI and OCO-2 at nonurban target locations around the world (see Figure 4). Subpanels represent different levels of screening and corrections for illumination and wavelength, with midday data reported on the top row (a and b) and length-of-day corrected data on the bottom row. (a) All uncorrected data. (b) Uncorrected data for 2018 only. (c) Length-of-day corrected data for 2018. (d) Same as in (c) but for phase angle differences limited to 20°. (e) Same as in (d) but for targets with uniform vegetation (single IGBP land cover >50% of total OCO-2 target area). Northern Forest combines evergreen needleleaf and mixed forest. All data are screened for clouds (clear days for OCO-2 and cld fraction <0.1 for TROPOMI). Note the change in scale between midday and length-of-day corrected data in the top row and bottom row.

overlapping in space and time of year but for different years (slope = 0.84 ± 0.051) and correlation ($R^2 = 0.69$; Figure 7a), with substantial improvement in slope for data overlapping in space and time for the same year of data (slope = 0.91 ± 0.045, $R^2 = 0.91$; Figure 7b). Correcting for illumination effects does not have much impact due to similarities in overpass time (midday for both; Figure 7c), but accounting for similar phase angles (Figure 7d) and locations with uniform vegetation (Figure 7e) leads to further improvement, as slope and r^2 converge on values of 1. However, we note a consistent offset of 0.1 W m^{-2} sr^{-1} nm−1 in TROPOMI relative to OCO-2 (negative bias) which is independent of SIF magnitude.

3.3. Retrieval Assessment: Comparison of GOME-2 SVD Methods to OCO-2 Targets

Figure 8 summarizes our assessment of accuracy of original GOME-2 retrievals (GOME2A-PKv1 and GOME2A-JJv28) against OCO-2 targets over the period 2015–2018. In the first case (not shown), the data sets are corrected for differences in overpass time and wavelength. In the second case, shown in Figure 8, data are also screened for clouds (effective cloud fraction < 0.3 for GOME-2), nonurban locations, and uniform vegetation. The first case already produces high agreement between GOME2A-PKv1 and OCO-2, with regression slope close to one (0.924 ± 0.059) and $R^2 = 0.72$. The GOME2A-JJv28 retrieval shows lower slope (0.539 ± 0.69) and $R^2 = 0.27$. Additional screening in the second case produces marginal improvement for GOME2A-PKv1, with slope and R^2 increasing to 0.953 ± 0.06 and 0.80, respectively, but significant improvement in GOME2A-JJv28, with slope and R^2 increasing to 0.704 ± 0.087 and 0.46. While long-term global comparisons (Figure 2 and 3) indicate a high bias in GOME2A-PKv1, the comparison at cloud-free OCO-2 targets with uniform vegetation indicates high SNR and accuracy. We note that the R^2 values do not account for retrieval uncertainty, which is much higher for GOME2-JJv28 due to the shorter retrieval window, and thus do not reflect differences in retrieval accuracy.

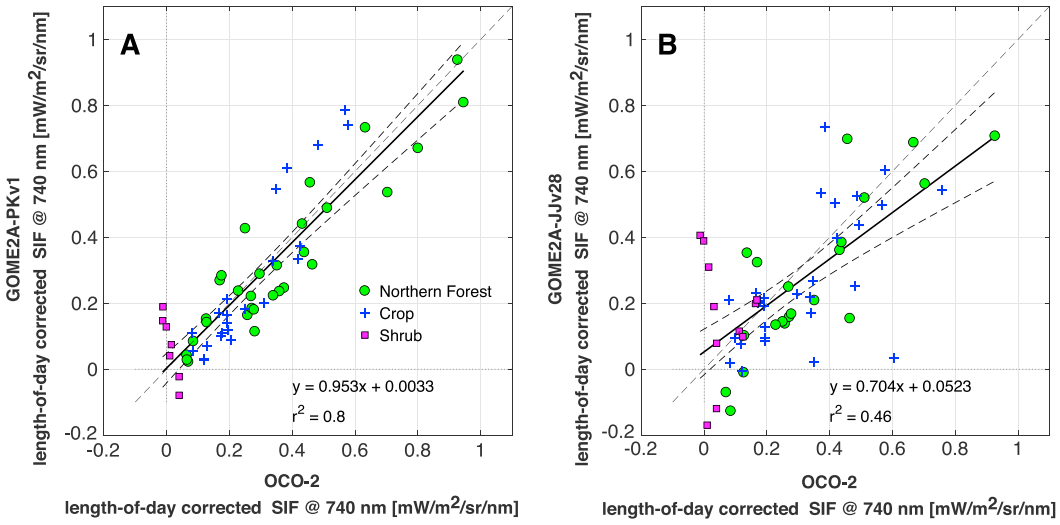

Figure 8. Analysis of daily, length-of-day corrected GOME-2 retrievals against OCO-2 targets over the period 2015–2018. Data sets are screen for clouds and normalized for wavelength (740 nm). We consider only nonurban locations with uniform vegetation.

We also note that the SIF variability of shrubs is much more significant in GOME-2 compared to OCO-2, while variability of forest and crops is similar in magnitude. This highlights the important effect of different sampling strategies on observed SIF variability. Even though uncertainties of GOME-2 and OCO-2 SIF for single soundings are very similar, the reason for the lower variability in OCO-2 SIF in low SIF landscapes is most likely related to the narrow swath of OCO-2 (~10 km), which provides more soundings per area and results in a substantially reduced standard error (1/sqrt(n)) compared to GOME-2. Therefore, we expect that a higher spread for GOME-2 in shrub landscapes, and low SIF emission landscapes in general, where precision is driven by the retrieval error and number of measurements. It is also worth considering that shrub landscapes are very heterogeneous, such that coarse GOME-2 footprints contain signals from other biomes not affecting small OCO-2 footprints (Wang et al., 2019).

3.4. Retrieval Sensitivity Analysis: Comparison of GOME-2 SVD Experiments to TROPOMI at Global Scale

GOME-2 retrieval sensitivity experiments are performed using instantaneous values at global scale for July 2018. Comparisons to TROPOMI are made for vegetated grid boxes, and exclude land cover classified as "Urban and Built-Up, "Snow and Ice," and "Barren or Sparsely Vegetated." We note that instantaneous values are expected to produce divergence in slope from the 1:1 relationship due to differences in time of day of GOME-2 (morning) and TROPOMI (midday). We know from diurnally resolved SIF observations across multiple ecosystems in North America (e.g., Magney, Bowling, et al., 2019; Yang et al., 2015, 2018) that SIF generally increases with light from midmorning (~9:30 am) to midday (~1:30 pm) in midsummer. An optimal regression should thus produce slope less than 1 with high correlation and zero y intercept.

Figure 9a shows results using the original GOME-2 retrieval (GOME2A-PKv1), representing the widest fitting window across all available methods and experiments (720–758 nm). The wide fitting window leads to reduced noise and high correlation ($R^2 = 0.77$) compared to smaller fitting windows (discussed below). This also produces the known high bias in absolute values (relative to TROPOMI), as indicated by high y intercept (0.33), which occurs despite the use of morning values.

Confining the retrieval window to 734–758 nm (Figure 9b) and 742–758 nm (Figure 9c) reduces the bias substantially (intercept = 0.12 and 0.06, respectively) but with reduced correlation ($R^2 = 0.74$ and 0.65). This is attributed to the use of fewer spectral points in narrower fitting windows, thus reducing SNR.

The choice of the SIF reference shape has a negligible impact on results. Spectra obtained from leaf level data instead of SCOPE have the very minor effect of a decreasing bias and an increasing slope. This finding is consistent for both the wide (720–758 nm; Figure 9a versus 9d) and the shorter (734–758 nm; Figure 9b versus

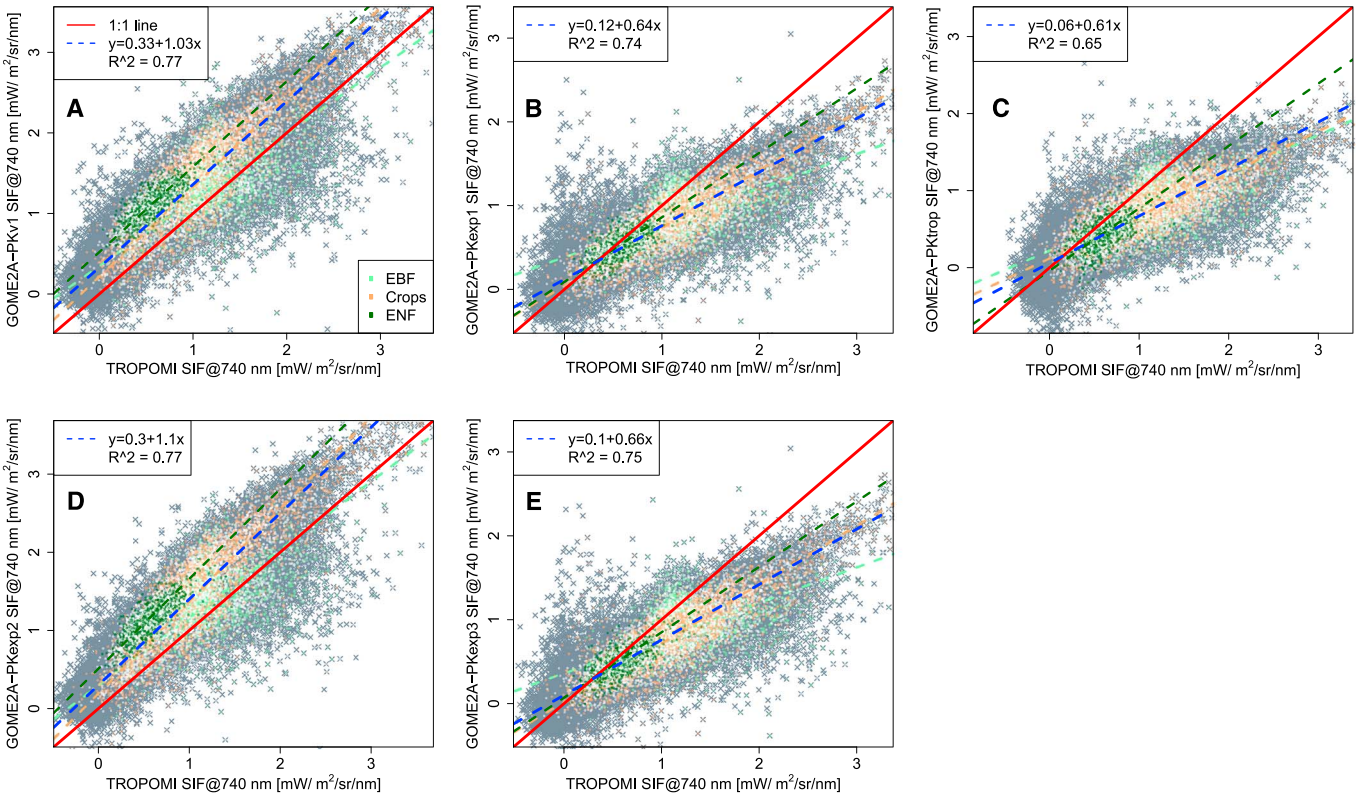

Figure 9. GOME-2 SIF retrieval sensitivity experiments. This shows the regression of global, vegetated, instantaneous retrieval values in July 2018 for GOME-2 (*y* axis) and TROPOMI (*x* axis). The top row shows GOME-2 retrievals using SIF reference shapes obtained from SCOPE simulations using varying retrieval windows including (a) 720–758 nm for PKv1, (b) 734–758 nm for PKexp1, and (c) 742–758 nm for PKtrop. Experiments in the bottom row (e and f; PKexp2 and PKexp3) use the same retrieval windows as the top row (a and b) but with SIF reference shapes obtained from the average of leaf level observations across multiple species (Magney, Frankenberg, et al., 2019).

9e) fitting windows. We also find very weak biome dependence for evergreen broadleaf forests, evergreen needleleaf forests, and crops (see color coding in Figure 9). In general, confining the retrieval window to that used by TROPOMI reduces intercept and bias at the cost of SNR.

4. Ongoing Challenges

Careful treatment of intersensor differences in overpass time, observed wavelength, cloud contamination, Sun-sensor geometry, and footprint area produces encouraging results for spaceborne SIF. Here we account for (1) **overpass time** using the length-of-day and solar zenith angle corrections, (2) **wavelength** using the ratio of wavelength ratios determined from leaf level spectral shapes, (3) **clouds** using observations of cloud optical depth and cloud fraction to screen for clear-sky conditions, (4) **Sun-sensor geometry** by examining similar phase angles (i.e., similar alignment of viewing and solar viewing angles) to ensure sensors observed the same (shaded or sunlit) scene, and (5) **footprint area** by examining scenes with uniform vegetation as determined from land cover data.

After accounting for these effects, we find high agreement of OCO-2 with ground-based observations at a subalpine evergreen needleleaf forest, and high agreement of GOME-2 and TROPOMI with nonurban OCO-2 targets across mostly northern temperate and high-latitude forests, crops, and shrubs. However, two well-established SVD retrieval methods for GOME-2 show substantial differences from each other in spatial variability in comparison to OCO-2 targets, and pronounced differences in magnitude at global scale compared to TROPOMI and OCO-2. The remaining uncertainty due to retrieval method, and other effects including radiometric calibration and spatial mismatch, is discussed below.

4.1. Retrieval Methodology

Retrieval experiments show high sensitivity to retrieval window and weak sensitivity to the reference SIF spectral shape (Figure 9). Specifically, all three experiments with reduced retrieval window size (GOME2A-PKexp1, GOME2A-PKexp2, GOME2A-PKtrop) compared to GOME2A-PKv1 show reduced magnitude in closer agreement with TROPOMI, but at a significant cost of reduced SNR and degradation of regression slope from a value close to 1 ($y = 0.71x + 0.28$) to well below the one-to-one line (slope ranging from 0.71 to 0.75). Thus, more analysis of the following factors is needed to understand retrieval effects in the far-red, including (1) SIF spectral shapes, (2) background reflectance, and (3) water vapor absorption by partial clouds. Future comparisons to new Photospec observations at the Old Black Spruce forest in southern Saskatchewan, Canada, which is characterized by more uniform vegetation and landscape features than Niwot Ridge, will facilitate assessment of these other effects.

4.2. Calibration Drift

A primary challenge to merging of SIF data sets for analysis of long-term variability is the presence of calibration drift affecting MetOp-A and MetOp-B GOME-2 sensors as well as other sensors. This drift produces a strong and widespread decreasing trend caused by instrument degradation (https://avdc.gsfc.nasa.gov/pub/data/satellite/MetOp/GOME_F/README_GOME-F_v26-v27.pdf GOME-2 FLOURESCENCE README FILE) if not fully accounted for. This is particularly troublesome given that GOME-2 provides our longest active record of SIF and provides the primary link between older records from SCIAMACHY and newer records from OCO-2 and TROPOMI. The use of OCO-2 to anchor the production of a long-term calibrated time series requires a correction to this calibration drift, focusing on a deeper investigation of raw L1B data. Making use of the most recent calibration information provided by the L1B data producers will help address issues such as degradation in solar irradiances and nonlinear trends in normalized radiances that can be deduced for example in ice radiances.

Changes in reflectance due to calibration drift may cause corresponding changes in the amount of cloudy data that are included in gridded averages, contributing to false trends. Accounting for this trend will require more detailed analysis and screening of clouds, perhaps using VIIRS and MODIS data together. Joint analysis of MODIS reflectance data can also help identify diverging anomalies related to clouds, time of day drift, geometry and swath width change (e.g., change in footprint size in GOME2A in July 2013), and other confounding factors.

4.3. South Atlantic Anomaly

The South Atlantic Anomaly exposes orbiting satellites to increased flux of energetic particles resulting in increased SIF measurement noise in southeastern portions of South America (Köhler et al., 2015; Joiner et al., 2016). The South Atlantic Anomaly has a substantial effect on GOME-2 radiances, small but nonnegligible impacts on SCIAMACHY, and almost no effect on TROPOMI (Kohler, Frankenberg et al., 2018). Joiner et al. (2016) mitigate, but do not completely eliminate, this effect in GOME-2 and SCIAMACHY by performing quality control checks on radiance outliers and reconstructed spectra derived from a reduced number of PCs.

4.4. Zero-Level Adjustment

Nonlinear effects such as dark current, stray light, temperature-related changes in the instrument response function, rotational-Raman scattering (effects may be significant at large solar and viewing angles), and memory effects produce false in-filling of solar Fraunhofer lines which have significant impacts on far-red SIF retrievals and which lead to biases on the order of 0.1 mW m^{-2} sr^{-1} nm^{-1} or greater, and which vary with latitude (Köhler et al., 2015; Joiner et al., 2012, 2016). These zero-level offsets are present in GOME-2 and SCIAMACHY retrievals and are not well captured by principal component analysis technique. Joiner et al. (2016) developed an empirical correction by constructing a regression model from a subset of retrievals over nonemitting ocean and desert surfaces. Zero-level adjustments remove a few tenths of a mW m^{-2} sr^{-1} nm^{-1} but do not completely remove biases at high radiance levels. Zero-level offsets are also observed in GOSAT and OCO-2 O2-A bands and are removed by analyzing SIF retrievals over nonemitting surfaces (Antarctica for OCO-2 and GOSAT high-gain spectra and Sahara for GOSAT medium-gain spectra; Christian Frankenberg, Fisher, et al., 2011).

5. Applications

Although calibration methods as suggested above are likely to produce more consistent time series across sensors, there remains the issue of spatial and temporal data gaps, footprint differences, and noise for individual sensors. This challenges efforts to assess long-term change, especially at subregional scale. Several efforts, discussed in more detail below, have been made in recent years to spatially downscale existing satellite SIF to higher temporal and spatially continuous resolutions, using either light use efficiency models or statistical methods, for more complete end-to-end SIF products, thus directly addressing this issue. All recently published methods use ancillary vegetation reflectance data from the MODerate-resolution Imaging Spectroradiometer (MODIS) as explanatory variables for SIF to predict or extrapolate SIF from either OCO-2 or GOME-2 in unobserved regions, taking advantage of empirical evidence that much of the variability in SIF is related to the fraction of PAR, as well as the stable long record (2000 to present) and high spatial resolution (~1 km) needed for downscaling and long-term prediction.

For example, Duveiller and Cescatti (2016) use a light use efficiency model to empirically link GOME-2 SIF with MODIS-based Normalized Difference Vegetation Index and other MODIS-derived parameters, to predict SIF at 0.05°. This approach is nice in the simplicity of the light use efficiency mechanistic equation, and the strict use of satellite observations of vegetation (Normalized Difference Vegetation Index) and environmental parameters (land surface temperature and evapotranspiration) to drive the model. Another product derived from GOME-2 SIF uses a neural network approach with MODIS reflectance to reconstruct GOME-2 SIF from independent estimates of PAR (denoted RSIF) every eight days at 0.5° (Gentine & Alemohammad, 2018). Both methods show consistency with tower-derived GPP data.

More recently (but in the same calendar year; Zhang, Joiner, Alemohammad et al., 2018) produced a global spatially contiguous solar-induced fluorescence data set, denoted CSIF, by training a neural network with surface reflectance data from the entire MODIS record (2000–2017) and two years of SIF (2015–2016) from OCO-2. The resulting maps are generated every four days at 0.05°, globally, for nearly two decades (2000–2016), providing unprecedented spatial and temporal coverage of long-term variability. Although this product is trained on only a couple years of OCO-2 data, and thus misses out on a more complete range of climate states, independent validation against GOME-2 and eddy covariance tower data shows high reproducibility of seasonal and spatial information. Yu et al. (2018) produced a similar product (global, 16-day, 0.05°) using a neural network trained on OCO-2 SIF data and MODIS reflectance, but focusing more on in-filling of OCO-2 gap regions and accurately preserving spatiotemporal patterns of the original SIF training data set. This product is trained with MODIS BDRF-corrected seven-band surface reflectance along OCO-2 orbits with spatial predictions stratified by biome and time step to optimize spatial variability along bioclimatic gradients. These data show high consistency with independent CFIS airborne data.

6. Discussion

Coordinated research focused on reconciliation of an already extensive and multidecadal spaceborne SIF record with well-characterized uncertainty and error quantification is critically needed. Despite substantial publication of individual SIF data sets (Christian Frankenberg, Fisher, et al., 2011; Joiner et al., 2013, 2014; Köhler, Frankenberg, et al., 2018; Köhler, Guanter, et al., 2018; Köhler et al., 2015), there exists known biases in current SIF products, and there has been no concerted effort to compare or cross-calibrate both retrieval algorithms and postprocessing strategies, such as the choice of reference targets or solar spectra. Thus, it is currently difficult to evaluate how inconsistencies across products affect scientific interpretation.

Recent and ongoing validation against ground and airborne SIF observations suggest that OCO-2 provides one of the more robust and practical options to optimize the sampling strategies of GOME-2, GOSAT, and TROPOMI, with the ultimate objective to anchor the production of a longer and spatially continuous SIF time series traceable to canopy measurements. Here we provide evidence supporting the use of OCO-2 target data as a promising benchmark to validate and calibrate diverse satellite sensors, and emphasize that careful attention is needed to account for key instrument differences such as time of day, wavelength, Sun-sensor

geometry, cloud effects, and footprint area through screening and corrections, and thus optimize consistency across instruments.

Specifically, we find that GOME-2 and TROPOMI perform exceedingly well in capturing spatial, seasonal, and interannual variability across OCO-2 targets, but that GOME-2 retrieval methods differ from each other in signal-to-noise and magnitude. Magnitude differences are attributed in part to the choice of retrieval window, but substantial research is needed to understand these sensitivities, and to validate consistency of methods and screening criteria, retrieved seasonal amplitudes for spectrally coarse sensors, and provide radiometric calibration and bias corrections.

TROPOMI is providing unprecedented spatial and temporal coverage at high resolution with nearly continuous mapping. The high precision and apparent accuracy of OCO-2 and TROPOMI retrievals suggests that these data sets will provide important benchmarks to help reconcile retrieval algorithm differences for moderate spectral resolution products, and identify and correct for sensor degradation that is responsible for drift in GOME-2 sensor radiance/irradiance records. Moreover, the rapidly expanding network of tower and airborne measurements will continue to provide important cal/val opportunities across diverse biomes around the world. Consequently, the prospect of leveraging ongoing OCO-2 and TROPOMI data, to anchor the calibration of overlapping sensors from GOME-2 and GOSAT, back-calibration of historical measurements from GOME and SCIAMACHY, and production of a long-term consistent time series of SIF, is extremely promising. Such a coordinated effort will facilitate (1) long-term record keeping of plant structural/functional change including improved observational constraint for model-data and data-data fusion, (2) analysis of climate sensitive regions through improved global coverage, and (3) identification of hot spots to focus field campaigns.

Efforts are under way to provide existing SIF products with common format, data structure, variables, corrections, and screening to correct individual sensors for differences in instantaneous illumination, Sun-sensor geometry, wavelength, and clouds to ensure consistency and facilitate cross-sensor comparisons. These reformatted data sets will undergo ongoing updates and continue to be disseminated to the global community via public servers (ftp://fluo.gps.caltech.edu). Site extraction tools are also available on GitHub and coded for open-source software such as R, providing seamless analysis of multiple sensors at locations specified by the user and a pathway for users to provide feedback to data providers.

7. Conclusions

SIF has been retrieved from multiple satellites with nearly coninuous global coverage since 1996, providing an unprecendented record for studying long-term photosynthetic change. However, no single instrument offers a long-term continuous running time series over this period, and differences in instrument characteristics and retrieval methodology have produces substantial variation across products, thus hindering long-term multisensor analyses. We leverage recently available data from state-of-the-art OCO-2 and TROPOMI instruments, and overlap with the spectrally coarse but longer-running GOME-2 instrument, in a first attempt to reconcile inconsistencies in the long-term record. We emphasize that OCO-2 SIF offers a key benchmarking data set for cross-sensor calibration due to its traceability to tower and airborne sensors, as demonstrated in this and previous studies. We also stress that careful screening and correction for key instrument differences increases consistency and reduces variability across products, and thus is a prerequisite for OCO-2-based calibration efforts.

The combination of screening, and focus on spatially resolved OCO-2 targets at locations with uniform vegetation, reveals surprising agreement of spatial, seasonal, and interannual variability between sensors. Comparison to OCO-2 also helps to address differences in signal-to-noise and magnitude resulting from retrieval method, and to understand sensitivities to retrieval window, atmospheric absorption, and reflectance. Retrieval sensitivity experiments here indicate that retrieval window choice largely explains magnitude differences between GOME-2 products. We conclude that next-generation sensors such as OCO-2 and TROPOMI have opened up the possibility to produce a multidecadal SIF record with well-characterized uncertainty and error quantification for overlapping instruments, enabling back-calibration of previous instruments and production of a longer and spatially continuous time series.

Acknowledgments

We thank Greg Ostermann for setting up the OCO-2 target selections. The data sets generated and/or analyzed for the current study are available at data repositories hosted at the Goddard Space Flight Center (https://avdc.gsfc.nasa.gov/pub/data/satellite/), the California Institute for Technology (airborne and satellite data here: ftp://fluo.gps.caltech.edu/data/, Photospec data here: https://data.caltech.edu/records/1231). A portion of these data were produced by the OCO-2 project at the Jet Propulsion Laboratory, California Institute of Technology, and obtained from the OCO-2 data archive maintained at the NASA Goddard Earth Science Data and Information Services Center. A portion of this research was carried out at the Jet Propulsion Laboratory, California Institute of Technology, under contract with NASA. Support from the Earth Science Division MEaSUREs program is acknowledged.

References

Baker, N. R. (2008). Chlorophyll fluorescence: A probe of photosynthesis in vivo. *Annual Review of Plant Biology*, *59*(1), 89–113. https://doi.org/10.1146/annurev.arplant.59.032607.092759

Cogliati, S., Rossini, M., Julitta, T., Meroni, M., Schickling, A., Burkart, A., et al. (2015). Continuous and long-term measurements of reflectance and Sun-induced chlorophyll fluorescence by using novel automated field spectroscopy systems. *Remote Sensing of Environment*, *164*, 270–281. https://doi.org/10.1016/j.rse.2015.03.027

Crisp, D., Atlas, R., Breon, F. M., Brown, L., Burrows, J., Ciais, P., et al. (2004). The Orbiting Carbon Observatory (OCO) mission. *Advances in Space Research*, *34*(4), 700–709. https://doi.org/10.1016/j.asr.2003.08.062

Daumard, F., Champagne, S., Fournier, A., Goulas, Y., Ounis, A., Hanocq, J. F., & Moya, I. (2010). A field platform for continuous measurement of canopy fluorescence. *IEEE Transactions on Geoscience and Remote Sensing*, *48*(9), 3358–3368. https://doi.org/10.1109/TGRS.2010.2046420

Duveiller, G., & Cescatti, A. (2016). Spatially downscaling Sun-induced chlorophyll fluorescence leads to an improved temporal correlation with gross primary productivity. *Remote Sensing of Environment*, *182*, 72–89. https://doi.org/10.1016/j.rse.2016.04.027

Fischer, J., Cordes, W., Schmitz-Peiffer, A., Renger, W., Mörl, P., Grassl, H., & Fisher, J. (1991). Detection of cloud-top height from backscattered radiances within the oxygen A band. Part 2: Measurements. *Journal of Applied Meteorology*, *30*(9), 1245–1259. https://doi.org/10.1175/1520-0450(1991)030<1245:DOCTHF>2.0.CO;2

Flexas, J., Escalona, J. M., Evain, S., Gulías, J., Moya, I., Osmond, C. B., & Medrano, H. (2002). Steady-state chlorophyll fluorescence (Fs) measurements as a tool to follow variations of net CO_2 assimilation and stomatal conductance during water-stress in C3 plants. *Physiologia Plantarum*, *114*(2), 231–240. https://doi.org/10.1034/j.1399-3054.2002.1140209.x

Frankenberg, C., Butz, A., & Toon, G. C. (2011). Disentangling chlorophyll fluorescence from atmospheric scattering effects in O_2 A-band spectra of reflected sun-light. *Geophysical Research Letters*, *38*, L03801. https://doi.org/10.1029/2010GL045896

Frankenberg, C., Drewry, D., Geier, S., Verma, M., Lawson, P., Stutz, J., & Grossmann, K.. (2016). Remote sensing of solar induced chlorophyll fluorescence from satellites, airplanes and ground-based stations. pp. 1707–10 in *Geoscience and Remote Sensing Symposium (IGARSS), 2016 IEEE International*.

Frankenberg, C., O'Dell, C., Guanter, L., & McDuffie, J. (2012). remote sensing of near-infrared chlorophyll fluorescence from space in scattering atmospheres: Implications for its retrieval and interferences with atmospheric CO_2 retrievals. *Atmospheric Measurement Techniques*, *5*(8), 2081–2094. https://doi.org/10.5194/amt-5-2081-2012

Frankenberg, C., Fisher, J. B., Worden, J., Badgley, G., Saatchi, S. S., Lee, J.-E., et al. (2011). New global observations of the terrestrial carbon cycle from GOSAT: Patterns of plant fluorescence with gross primary productivity. *Geophysical Research Letters*, *38*, L17706. https://doi.org/10.1029/2011GL048738

Frankenberg, C., Köhler, P., Magney, T. S., Geier, S., Lawson, P., Schwochert, M., et al. (2018). The Chlorophyll Fluorescence Imaging Spectrometer (CFIS), mapping far red fluorescence from aircraft. *Remote Sensing of Environment*, *217*, 523–536. https://doi.org/10.1016/j.rse.2018.08.032

Frankenberg, C., O'Dell, C., Berry, J., Guanter, L., Joiner, J., Köhler, P., et al. (2014). Prospects for chlorophyll fluorescence remote sensing from the Orbiting Carbon Observatory-2. *Remote Sensing of Environment*, *147*, 1–12. https://doi.org/10.1016/j.rse.2014.02.007

Gentine, P., & Alemohammad, S. H. (2018). Reconstructed solar-induced fluorescence: A machine learning vegetation product based on MODIS surface reflectance to reproduce GOME-2 solar-induced fluorescence. *Geophysical Research Letters*, *45*, 3136–3146. https://doi.org/10.1002/2017GL076294

Genty, B., Briantais, J.-M., & Baker, N. R. (1989). The relationship between the quantum yield of photosynthetic electron transport and quenching of chlorophyll fluorescence. *Biochimica et Biophysica Acta (BBA) - General Subjects*, *990*(1), 87–92. https://doi.org/10.1016/S0304-4165(89)80016-9

Grossmann, K., Frankenberg, C., Magney, T. S., Hurlock, S. C., Seibt, U., & Stutz, J. (2018). PhotoSpec: A new instrument to measure spatially distributed red and far-red solar-induced chlorophyll fluorescence. *Remote Sensing of Environment*, *216*, 311–327. https://doi.org/10.1016/j.rse.2018.07.002

Guanter, L., Aben, I., Tol, P., Krijger, J. M., Hollstein, A., Köhler, P., et al. (2015). Potential of the TROPOspheric Monitoring Instrument (TROPOMI) onboard the Sentinel-5 precursor for the monitoring of terrestrial chlorophyll fluorescence. *Atmospheric Measurement Techniques*, *8*(3), 1337–1352. https://doi.org/10.5194/amt-8-1337-2015

Guanter, L., Frankenberg, C., Dudhia, A., Lewis, P. E., Gómez-Dans, J., Kuze, A., et al. (2012). Retrieval and global assessment of terrestrial chlorophyll fluorescence from GOSAT space measurements. *Remote Sensing of Environment*, *121*, 236–251. https://doi.org/10.1016/j.rse.2012.02.006

Hilker, T., Lyapustin, A. I., Hall, F. G., Myneni, R., Knyazikhin, Y., Wang, Y., et al. (2015). On the measurability of change in Amazon vegetation from MODIS. *Remote Sensing of Environment*, *166*, 233–242. https://doi.org/10.1016/j.rse.2015.05.020

Joiner, J., Guanter, L., Lindstrot, R., Voigt, M., Vasilkov, A. P., Middleton, E. M., et al. (2013). Global monitoring of terrestrial chlorophyll fluorescence from moderate spectral resolution near-infrared satellite measurements: Methodology, simulations, and application to GOME-2. *Atmospheric Measurement Techniques Discussions*, *6*(2), 3883–3930. https://doi.org/10.5194/amtd-6-3883-2013

Joiner, J., Yoshida, Y., Guanter, L., & Middleton, E. M. (2016). New methods for retrieval of chlorophyll red fluorescence from hyperspectral satellite instruments: simulations and application to GOME-2 and SCIAMACHY. *Atmospheric Measurement Techniques*, *9*, 3939–3967. https://www.atmosmeas-tech.net/9/3939/2016

Joiner, J., Yoshida, Y., Vasilkov, A. P., Schaefer, K., Jung, M., Guanter, L., et al. (2014). The seasonal cycle of satellite chlorophyll fluorescence observations and its relationship to vegetation phenology and ecosystem atmosphere carbon exchange. *Remote Sensing of Environment*, *152*, 375–391. https://doi.org/10.1016/j.rse.2014.06.022

Joiner, J., Yoshida, Y., Vasilkov, A. P., Yoshida, Y., Corp, L. A., & Middleton, E. M. (2011). First observations of global and seasonal terrestrial chlorophyll fluorescence from space. *Biogeosciences*, *8*(3), 637–651. https://doi.org/10.5194/bg-8-637-2011

Joiner, J., Yasuko, Y., Vasilkov, A. P., Middleton, E. M., Campbell, P. K. E., & Kuze, A. (2012). Filling-in of near-infrared solar lines by terrestrial fluorescence and other geophysical effects: Simulations and space-based observations from SCIAMACHY and GOSAT. *Atmospheric Measurement Techniques*, *5*(4), 809–829. https://doi.org/10.5194/amt-5-809-2012

Köhler, P., Guanter, L., & Joiner, J. (2015). A linear method for the retrieval of Sun-induced chlorophyll fluorescence from GOME-2 and SCIAMACHY data. *Atmospheric Measurement Techniques*, *8*(6), 2589–2608. https://doi.org/10.5194/amt-8-2589-2015

Köhler, P., Frankenberg, C., Magney, T. S., Guanter, L., Joiner, J., & Landgraf, J. (2018). Global retrievals of solar-induced chlorophyll fluorescence with TROPOMI: First results and intersensor comparison to OCO-2. *Geophysical Research Letters*, *45*, 10,456–10,463. https://doi.org/10.1029/2018GL079031

Köhler, P., Guanter, L., Kobayashi, H., Walther, S., & Yang, W. (2018). Assessing the potential of Sun-induced fluorescence and the canopy scattering coefficient to track large-scale vegetation dynamics in Amazon forests. *Remote Sensing of Environment*, *204*, 769–785. https://doi.org/10.1016/j.rse.2017.09.025

Krause, G. H., & Weis, E. (1991). Chlorophyll fluorescence and photosynthesis: The basics. *Annual Review of Plant Biology*, *42*(1), 313–349. https://doi.org/10.1146/annurev.pp.42.060191.001525

Liu, L., Liu, X., Wang, Z., & Zhang, B. (2016). Measurement and analysis of bidirectional SIF emissions in wheat canopies. *IEEE Transactions on Geoscience and Remote Sensing*, *54*(5), 2640–2651. https://doi.org/10.1109/TGRS.2015.2504089

MacBean, N., Maignan, F., Bacour, C., Lewis, P., Peylin, P., Guanter, L., et al. (2018). Strong constraint on modelled global carbon uptake using solar-inducedchlorophyll fluorescence data. *Scientific Reports*,, *8*(1, 1973. https://doi.org/10.1038/s41598-018-20024-w

Maeda, E. E., & Galvão, L. S. (2015). Sun-sensor geometry effects on vegetation index anomalies in the Amazon rainforest. *GIScience & Remote Sensing*, *52*(3), 332–343. https://doi.org/10.1080/15481603.2015.1038428

Magney, T. 2019. Canopy and needle scale fluorescence data from Niwot Ridge, Colorado 2017–2018 (version 0.1) [Data set]. CaltechDATA. https://doi.org/10.22002/d1.1231

Magney, T. S., Bowling, D. R., Logan, B., Grossmann, K., Stutz, J., Blanken, P., et al. (2019). Mechanistic evidence for tracking the seasonality of photosynthesis with solar-induced fluorescence. *Proceedings of the National Academy of Sciences*, *116*(24), 11,640–11,645.

Magney, T. S., Frankenberg, C., Khler, P., North, G., Davis, T. S., Dold, C., et al. (2019). Disentangling changes in the spectral shape of chlorophyll fluorescence: implications for remote sensing of photosynthesis. *Journal of Geophysical Research: Biogeosciences*, *124*, 1491–1507. https://doi.org/10.1029/2019JG005029

Migliavacca, M., Perez-Priego, O., Rossini, M., El-Madany, T. S., Moreno, G., van der Tol, C., et al. (2017). Plant functional traits and canopy structure control the relationship between photosynthetic CO_2 uptake and far-red Sun-induced fluorescence in a Mediterranean grassland under different nutrient availability. *New Phytologist*, *214*(3), 1078–1091. https://doi.org/10.1111/nph.14437

Morton, D. C., Nagol, J., Carabajal, C. C., Rosette, J., Palace, M., Cook, B. D., et al. (2014). Amazon forests maintain consistent canopy structure and greenness during the dry season. *Nature*, *506*(7487), 221–224. https://doi.org/10.1038/nature13006

Moya, I., Camenen, L., Evain, S., Goulas, Y., Cerovic, Z. G., Latouche, G., et al. (2004). A new instrument for passive remote sensing: 1. Measurements of Sunlight-induced chlorophyll fluorescence. *Remote Sensing of Environment*, *91*(2), 186–197. https://doi.org/10.1016/j.rse.2004.02.012

Norton, A. J., Rayner, P. J., Koffi, E. N., & Scholze, M. (2018). Assimilating solar-induced chlorophyll fluorescence into the terrestrial biosphere model BETHYSCOPE v1.0: model description and information content. *Geoscientific Model Development*, *11*, 1517–1536. https://doi.org/10.5194/gmd-11-1517-2018

O'Dell, C. W., Connor, B., Bösch, H., O'Brien, D., Frankenberg, C., Castano, R., et al. (2012). The ACOS CO_2 retrieval algorithm: Part 1—Description and validation against synthetic observations. *Atmospheric Measurement Techniques*, *5*(1), 99–121. https://doi.org/10.5194/amt-5-99-2012

Shan, N., Ju, W., Migliavacca, M., Martini, D., Guanter, L., Chen, J., et al. (2019). Modeling canopy conductance and transpiration from solar-induced chlorophyll fluorescence. *Agricultural and Forest Meteorology*, *268*, 189–201.

Sun, Y., Frankenberg, C., Wood, J. D., Schimel, D. S., Jung, M., Guanter, L., et al. (2017). OCO-2 advances photosynthesis observation from space via solar-induced chlorophyll fluorescence. *Science*, *358*(6360), eaam5747. https://doi.org/10.1126/science.aam5747

Sun, Y., Frankenberg, C., Jung, M., Joiner, J., Guanter, L., Köhler, P., & Magney, T. (2018). Overview of solar-induced chlorophyll fluorescence (SIF) from the Orbiting Carbon Observatory-2: Retrieval, cross-mission comparison, and global monitoring for GPP. *Remote Sensing of Environment*, *209*(February), 808–823. https://doi.org/10.1016/j.rse.2018.02.016

Van Der Tol, C., Berry, J. A., Campbell, P. K. E., & Rascher, U. (2014). Models of fluorescence and photosynthesis for interpreting measurements of solar-induced chlorophyll fluorescence. *Journal of Geophysical Research: Biogeosciences*, *119*, 2312–2327. https://doi.org/10.1002/2014JG002713

Verma, M., Schimel, D., Evans, B., Frankenberg, C., Beringer, J., Drewry, D. T., et al. (2017). Effect of environmental conditions on the relationship between solar-induced fluorescence and gross primary productivity at an OzFlux grassland site. *Journal of Geophysical Research: Biogeosciences*, *122*, 716–733. https://doi.org/10.1002/2016JG003580

Verrelst, J., Schaepman, M. E., Koetz, B., & Kneubühler, M. (2008). Angular sensitivity analysis of vegetation indices derived from CHRIS/PROBA data. *Remote Sensing of Environment*, *112*(5), 2341–2353. https://doi.org/10.1016/j.rse.2007.11.001

Wang, C., Beringer, J., Hutley, L. B., Cleverly, J., Li, J., Liu, Q., & Sun, Y. (2019). Phenology dynamics of dryland ecosystems along North Australian tropical transect revealed by satellite solar-induced chlorophyll fluorescence. *Geophysical Research Letters*, *46*, 5294–5302. https://doi.org/10.1029/2019GL082716

Wood, J. D., Griffis, T. J., Baker, J. M., Frankenberg, C., Verma, M., & Yuen, K. (2017). Multiscale analyses of solar-induced florescence and gross primary production. *Geophysical Research Letters*, *44*, 533–541. https://doi.org/10.1002/2016GL070775

Yang, P., & van der Tol, C. (2018). Linking canopy scattering of far-red Sun-induced chlorophyll fluorescence with reflectance. *Remote Sensing of Environment*, *209*, 456–467. https://doi.org/10.1016/j.rse.2018.02.029

Yang, X., Shi, H., Stovall, A., Guan, K., Miao, G., Zhang, Y., et al. (2018). FluoSpec 2—An automated field spectroscopy system to monitor canopy solar-induced fluorescence. *Sensors (Switzerland)*, *18*(7).

Yang, X., Tang, J., Mustard, J. F., Lee, J.-e., & Rossini, M. (2015). Geophysical research letter supplementary information for "Solar-induced chlorophyll fluorescence correlates with canopy photosynthesis on diurnal and seasonal scales in a temperate deciduous forest". *Geophysical Research Letters*, *42*, 2977–2987. https://doi.org/10.1002/2015GL063201

Yu, L., Wen, J., Chang, C. Y., Frankenberg, C., & Sun, Y. (2018). High resolution global contiguous solar-induced chlorophyll fluorescence (SIF) of Orbiting Carbon Observatory-2 (OCO-2). *Geophysical Research Letters*, *46*, 1449–1458. https://doi.org/10.1029/2018GL081109

Zhang, Y., Joiner, J., Gentine, P., & Zhou, S. (2018). Reduced solar-induced chlorophyll fluorescence from GOME-2 during Amazon drought caused by dataset artifacts. *Global Change Biology*, 2229–2230.

Zhang, Y., Joiner, J., Alemohammad, S. H., Zhou, S., & Gentine, P. (2018). A global spatially contiguous solar-induced fluorescence (CSIF) Dataset using neural networks. *Biogeosciences*, *15*(19), 5779–5800. https://doi.org/10.5194/bg-15-5779-2018

Zhang, Y., Xiao, X., Zhang, Y., Wolf, S., Zhou, S., Joiner, J., et al. (2018). On the relationship between sub-daily instantaneous and daily total gross primary production: Implications for interpreting satellite-based SIF retrievals. *Remote Sensing of Environment*, *205*, 276–289. https://doi.org/10.1016/j.rse.2017.12.009